ATLAS CONF Note
ATLAS-CONF-2023-021
23rd March 2023

Search for pair production of squarks or gluinos decaying via sleptons or weak bosons in final states with two same-sign or three leptons with the ATLAS detector

The ATLAS Collaboration

A search for pair production of squarks or gluinos decaying via sleptons or weak bosons is reported. The search targets a final state with exactly two leptons with same-sign electric charge or at least three leptons without any charge requirement. The analysed dataset corresponds to an integrated luminosity of 139 fb^{-1} of proton–proton collisions collected at a centre-of-mass energy of 13 TeV with the ATLAS detector at the LHC. Multiple signal regions are defined targeting several SUSY simplified models yielding the desired final states. A unique control region is used to constrain the normalisation of the WZ+jets background. No significant excess of events over the Standard Model expectation is observed. The results are interpreted in the context of several supersymmetric models featuring R-parity conservation or R-parity violation, extending the exclusion limits from previous searches. In models considering gluino (squark) pair production, gluino (squark) masses are excluded up to 2.2 (1.7) TeV at 95% confidence level.

1 Introduction

The ATLAS experiment [1] at the Large Hadron Collider (LHC) [2] probes the electroweak sector of the Standard Model (SM) at the TeV scale. The presence of prompt electrons or muons (collectively referred to as leptons) in reconstructed events provides one of the main experimental signatures to isolate processes mediated by electroweak, scalar or exotic couplings, from the large QCD multijet background produced in proton-proton (pp) collisions. The production of pairs of leptons with the same electric charge (further referred to as same-sign leptons) is particularly rare in the SM, with an inclusive cross section at the level of 1 pb [3] for centre of mass energies around 13 TeV. By contrast, it may occur frequently in beyond-SM (BSM) extensions [4–6] and therefore searches for anomalous production of same-sign leptons have been integral parts of the LHC and Tevatron experimental programs [7–9].

Extensions of the SM introducing invariance under supersymmetric transformations [10–15] (SUSY) provide many such possibilities. Even minimal realisations such as the Minimal Supersymmetric Standard Model (MSSM) [16, 17] contain SUSY partners for all SM fields as well as members of an extended Higgs sector [18] that may decay in complex cascades involving leptons. In the MSSM, SUSY transformations relate each of the Weyl components of a fundamental SM chiral fermion f to a new scalar field, $\tilde{f}_{\mathrm{L}}$ or $\tilde{f}_{\mathrm{R}}$, with identical gauge charges. The quarks and leptons thus lead to 12 physical squarks ($\tilde{q}$) and 9 sleptons ($\tilde{\ell}$, $\tilde{\nu}$). Gluinos $\tilde{g}$ are the spin-1/2 Majorana fermionic partners of SM gluons. The partners of electroweak and Higgs bosons mix to form spin-1/2 mass eigenstates referred to as neutralinos $\tilde{\chi}^0_i$ ($i = 1, \ldots 4$, ordered by increasing mass) for the neutral ones, and as charginos $\tilde{\chi}^\pm_j$ ($j = 1, 2$) for the others. Depending on the dominant components in the admixtures, they might be qualified as bino-, wino- or higgsino-like, with important consequences on the mass spectrum and main decay channels [19].

By assuming an ad hoc discrete symmetry, the R-parity [20], the lightest SUSY particle (LSP) is stable and may contribute to Dark Matter [21, 22]. In many models the LSP is the lightest neutralino $\tilde{\chi}^0_1$, which interacts weakly and thus yields the characteristic signature of missing transverse momentum in the detector. Other phenomenological consequences in R-parity conserving (RPC) models include production of SUSY partners always in pairs, with decays in cascade to a final state of LSPs and SM particles. On the other hand, R-parity violating (RPV) models [23] may allow non-conservation of baryon or lepton numbers potentially necessary for grand unification [24] or neutrino flavour mixing. Detector signatures in such models are highly variable depending on the nature and strength of the non-zero RPV couplings; in particular direct couplings between (s)leptons and (s)quarks and/or gauginos are possible and can significantly enhance the production of multilepton final states at the LHC.

A search for pair production of gluinos or squarks with the ATLAS experiment is presented in the following. Different types of cascade decays are considered, arising either in SUSY RPC or RPV scenarios, which lead to final states with same-sign or three leptons, several jets, and missing transverse momentum when relevant. The analysis makes use of the full set of data collected during the Run 2 phase of the LHC operation. The results complete and improve over those from an earlier search [25] and performed on the same dataset, yielding increased sensitivity for two benchmark scenarios while also providing new tailored search regions for processes or decay modes not considered in Ref. [25], such as the production of squarks of first or second generation. A search of similar purpose was performed by the CMS experiment [26]. Models with squark production were previously probed by ATLAS during Run 1 [27].

The paper is organised as follows. A general overview of the ATLAS detector is provided in Section 2, followed in Section 3 by descriptions of the different SUSY processes of relevance. Details on the recorded data used for the analysis as well as the simulated Monte Carlo (MC) samples are given in Section 4, while the reconstruction of different types of high-level objects from those inputs is described in Section 5. The definitions of several search regions to look for the chosen SUSY processes are motivated in Section 6. The estimation of SM backgrounds is further explained in Section 7, completed by a summary of the sources of systematic uncertainty affecting background or signal predictions in Section 8. The various estimates are combined to observations in control and search regions within a coherent statistical framework described in Section 9, providing the results listed in Section 10 and exploited to perform hypothesis testing for the signal strength of the various SUSY benchmarks. Concluding remarks are provided in Section 11.

2 ATLAS detector

The ATLAS detector [1] at the LHC covers nearly the entire solid angle around the collision point.[1] It consists of an inner tracking detector surrounded by a thin superconducting solenoid, electromagnetic and hadron calorimeters, and a muon spectrometer incorporating three large superconducting air-core toroidal magnets.

The inner-detector system (ID) is immersed in a 2 T axial magnetic field and provides charged-particle tracking in the range $|\eta| < 2.5$. The high-granularity silicon pixel detector covers the vertex region and typically provides four measurements per track, the first hit normally being in the insertable B-layer (IBL) installed before Run 2 [28, 29]. It is followed by the silicon microstrip tracker (SCT), which usually provides eight measurements per track. These silicon detectors are complemented by the transition radiation tracker (TRT), which enables radially extended track reconstruction up to $|\eta| = 2.0$. The TRT also provides electron identification information based on the fraction of hits (typically 30 in total) above a higher energy-deposit threshold corresponding to transition radiation.

The calorimeter system covers the pseudorapidity range $|\eta| < 4.9$. Within the region $|\eta| < 3.2$, electromagnetic calorimetry is provided by barrel and endcap high-granularity lead/liquid-argon (LAr) calorimeters, with an additional thin LAr presampler covering $|\eta| < 1.8$ to correct for energy loss in material upstream of the calorimeters. Hadron calorimetry is provided by the steel/scintillator-tile calorimeter, segmented into three barrel structures within $|\eta| < 1.7$, and two copper/LAr hadron endcap calorimeters. The solid angle coverage is completed with forward copper/LAr and tungsten/LAr calorimeter modules optimised for electromagnetic and hadronic energy measurements respectively.

The muon spectrometer (MS) comprises separate trigger and high-precision tracking chambers measuring the deflection of muons in a magnetic field generated by the superconducting air-core toroidal magnets. The field integral of the toroids ranges between 2.0 and 6.0 T m across most of the detector. Three layers of precision chambers, each consisting of layers of monitored drift tubes, cover the region $|\eta| < 2.7$, complemented by cathode-strip chambers in the forward region, where the background is highest. The muon trigger system covers the range $|\eta| < 2.4$ with resistive-plate chambers in the barrel, and thin-gap chambers in the endcap regions.

Interesting events are selected by the first-level trigger system implemented in custom hardware, followed by selections made by algorithms implemented in software in the high-level trigger [30]. The first-level

---

[1] ATLAS uses a right-handed coordinate system with its origin at the nominal interaction point (IP) in the centre of the detector and the z-axis along the beam pipe. The x-axis points from the IP to the centre of the LHC ring, and the y-axis points upwards. Cylindrical coordinates (r, ϕ) are used in the transverse plane, ϕ being the azimuthal angle around the z-axis. The pseudorapidity is defined in terms of the polar angle θ as $\eta = -\ln\tan(\theta/2)$. Angular distance is measured in units of $\Delta R \equiv \sqrt{(\Delta\eta)^2 + (\Delta\phi)^2}$.

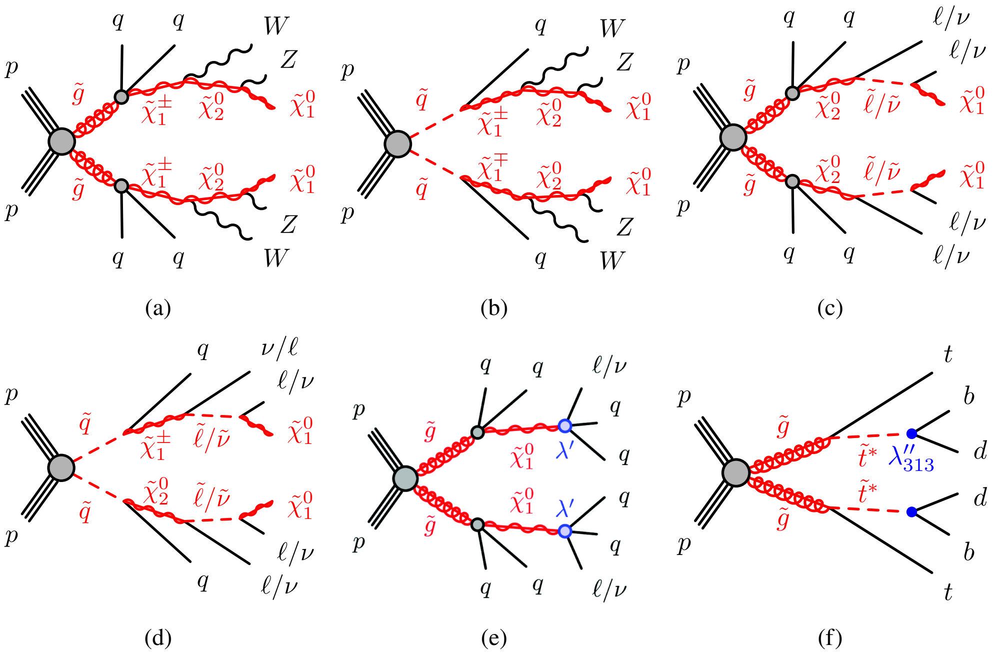

Figure 1: Examples of sources of same-sign leptons which may arise in supersymmetric processes and are targeted by the search regions of the analysis.

trigger accepts events from the 40 MHz bunch crossings at a rate below 100 kHz, which the high-level trigger further reduces in order to record events to disk at about 1 kHz.

An extensive software suite [31] is used in data simulation, in the reconstruction and analysis of real and simulated data, in detector operations, and in the trigger and data acquisition systems of the experiment.

3 Signal models

This analysis considers experimental signatures arising from the production of either gluino pairs or squark-antisquark pairs $\tilde{q}\tilde{q}^*$ (with $q = u, d, s, c$). Several gluino and squark decay modes are investigated, summarised in Figure 1: in most cases the first step of the decay is to a non-stable electroweak gaugino $\tilde{\chi}$ and SM quark(s) of first or second generation. Various $\tilde{\chi}$ decay modes may lead to final states featuring pairs of same-sign or three leptons. Amongst those possibilities, this analysis searches in particular for the following sources of electrons and muons:

- $\tilde{\chi}$ decays into SM gauge bosons and $\tilde{\chi}_1^0$ LSPs; while the direct decays $\tilde{\chi}_1^\pm \to W^\pm\tilde{\chi}_1^0$ and $\tilde{\chi}_2^0 \to Z\tilde{\chi}_1^0$ are most efficiently probed with other experimental signatures [32–34], more favourable branching ratio to same-sign leptons are found for cascade decays such as $\tilde{\chi}_1^\pm \to \tilde{\chi}_2^0 W^\pm \to \tilde{\chi}_1^0 Z W^\pm$, as illustrated in Figures 1(a) and 1(b), and thus the focus here.
- $\tilde{\chi}$ decays into sleptons and subsequently to SM leptons and $\tilde{\chi}_1^0$ LSPs, such as $\tilde{\chi}_1^\pm(\to \ell\tilde{\nu}/\tilde{\ell}\nu) \to \ell\nu\tilde{\chi}_1^0$ or $\tilde{\chi}_2^0(\to \tilde{\ell}\ell) \to \ell^+\ell^-\tilde{\chi}_1^0$, as illustrated in Figures 1(c) and 1(d).
- direct $\tilde{\chi}_1^0$ decay into SM leptons and quarks via a non-zero RPV coupling λ', $\tilde{\chi}_1^0 \to u\bar{d}\ell^+$, as illustrated in Figure 1(e).

- $\tilde{g} \to \bar{\tilde{t}}t \to \bar{t}bq$ decays via a non-zero RPV coupling λ'', shown in Figure 1(f).

The experimental sensitivity to such processes is assessed in simplified models [35–37] where only the superpartners directly involved in the process of interest are considered, alternative production and decay modes are ignored, and masses and mixings of superpartners are either varied freely or fixed to chosen values.

For the cascade decays of charginos into pairs of SM bosons (Figures 1(a), 1(b)), gluino (or squark) and $\tilde{\chi}_1^0$ LSP masses are varied independently to generate different scenarios. The masses of intermediate superpartners are then set halfway, $m(\tilde{\chi}_1^{\pm}) = (m(\tilde{g}/\tilde{q}) + m(\tilde{\chi}_1^0))/2$ and $m(\tilde{\chi}_2^0) = (m(\tilde{\chi}_1^{\pm}) + m(\tilde{\chi}_1^0))/2$. The decay of $\tilde{\chi}_1^{\pm}$ and $\tilde{\chi}_2^0$ to leptons takes place through real or virtual W/Z bosons depending on the mass difference with the LSP. Quarks produced in the first step of the gluino decay are assumed to be u, d, s or c with equal probability. Due to the small Yukawa couplings for the first two quark generations, the decays $\tilde{g} \to qq\tilde{\chi}_1^{\pm}$ and $\tilde{q} \to q\tilde{\chi}_1^{\pm}$ are only relevant for a wino-like chargino [38]; therefore, only production of left-squarks is considered. In minimal models with a neutralino LSP [38], such chargino cascade decays together with a non-degenerate mass hierarchy may occur when neutralinos are non-trivial admixtures but would compete with several other decay modes [19], generally more favourable. In gauge-mediated [39–41] SUSY breaking models (GMSB) however, this can be a more natural mode in the alternative form $\tilde{\chi}_1^{\pm} \to W^{\pm}\tilde{\chi}_1^0 \to W^{\pm}Z\tilde{G}$. Previous ATLAS searches with various signatures [25, 27, 42, 43] probed gluino masses up to 2 TeV and squark masses up to 630 GeV with these decay modes.

Similarly, for the decays of charginos and neutralinos into sleptons (Figures 1(c), 1(d)), gluino (or squark) and $\tilde{\chi}_1^0$ LSP masses are varied independently, while the masses of intermediate superpartners are set to $m(\tilde{\chi}_1^{\pm}/\tilde{\chi}_2^0) = (m(\tilde{g}/\tilde{q}) + m(\tilde{\chi}_1^0))/2$ and $m(\tilde{\ell}/\tilde{\nu}) = (m(\tilde{\chi}_1^{\pm}/\tilde{\chi}_2^0) + m(\tilde{\chi}_1^0))/2$. Such scenarios arise in mass spectra of models where sleptons are light, and as such have been searched for in early LHC analyses [44–46]. Gluinos are chosen to decay only into $\tilde{\chi}_2^0$ (and unlike other models, $\tilde{g} \to b\bar{b}\tilde{\chi}_2^0$ is open too), while squarks may decay equiprobably into either $\tilde{\chi}_1^{\pm}$ or $\tilde{\chi}_2^0$. In both cases, the gaugino subsequently decays equiprobably into any of the six SM leptons, together with the appropriate left-slepton considering charge and lepton number conservations. The latter decay exclusively into their SM partner and the LSP. Previous ATLAS searches [25, 27, 42, 43] probed gluino masses up to 2.2 TeV and squark masses up to 850 GeV. The intermediate charginos or sleptons are also constrained by previous analyses [47–50], but the present analysis can probe masses of these particles higher than the ones excluded by the direct production, thanks to the higher production rate in the cascade decays of gluinos or squarks.

Finally, event kinematics in the case of neutralino decays via λ' RPV couplings (Figure 1(e)) are completely determined by the gluino and $\tilde{\chi}_1^0$ LSP masses, which again are varied independently to generate different scenarios. Without choosing explicit values, it is assumed that the relevant λ' couplings can be large enough to allow for a prompt $\tilde{\chi}_1^0$ decay into $\ell^- u\bar{d}$ or $\nu_\ell d\bar{d}$ ($\ell = e, \mu$), or their charge conjugates, equiprobably, while evading low-energy experimental bounds [51]. The $\tilde{\chi}_1^0$ natural width also depends on the mass of virtual squarks mediating the decay and is set to 100 MeV. For such a scenario, current experimental sensitivity [52] reaches gluino masses up to 2.2 TeV.

An additional scenario exemplified in Figure 1(f) is considered, in which pair-produced gluinos decay into the lightest top squark (and a SM top) which itselfs decays via suitable λ'' RPV couplings into a pair of quarks, leading in half of the cases to a final state of two same-sign tops and up to four jets. Such scenarios were highlighted in particular in Ref. [53] and searches have been performed in the $\bar{t}\bar{t}bbqq$ [25, 26, 52] and $\bar{t}\bar{t}qqqq$ [54] final states. In the present analysis, only the former case is addressed, as it yields a clearer experimental signature; for this scenario, Ref. [52] excluded gluino masses up to 1.8 TeV for top squark masses around 1 TeV. A set of benchmark models is generated by varying gluino and top squark masses independently, the latter being bounded from below by existing constraints on $\tilde{t}\tilde{t}^*$ production [55]. The top squarks are assumed to decay promptly. A new set of search regions allows to extend the sensitivity beyond that reached by Ref. [25] with the same data.

4 Data and samples of simulated events

The results presented here are obtained by analysing proton–proton collision data collected during the Run 2 of LHC operation at a centre-of-mass energy of 13 TeV. The number of expected simultaneous inelastic interactions averages to 33.7 for the entire data set [56], while reaching beyond 70 in a small fraction of data collected in 2017 and 2018. Events recorded when parts of the detector were not functional or reserved for detector commissioning or calibration purposes are subsequently ignored, leaving 95.6% of the recorded data [56] available for analysis. The integrated luminosity for this combined data set amounts to 139 fb^{-1}, with an uncertainty of 1.7%. The latter is obtained [57] using the LUCID-2 detector [58] for the primary luminosity measurements.

Large samples of simulated events are also employed, mainly to predict contributions from SM processes with prompt[2] leptons to the regions of interest of the analysis, as well as those from hypothetical SUSY signal processes. Other usages include verifying assumptions of background estimate methods based on data, or more generally assessing systematic uncertainties. Those samples are obtained by simulating individual proton–proton collisions for hard-interaction processes of interest with different combinations of MC event generators described further on. The events are then processed through a detailed simulation of the ATLAS detector [59] based on GEANT4 [60]. In some cases, notably for BSM signal samples, a faster simulation which relies on a parameterisation of the calorimeter response [61] is used instead. At this stage, additional minimum-bias interactions simulated separately (see below) are overlaid onto the hard interaction. The response of the detector and its electronic readout chain is then emulated [59], also accounting for effects from interactions in the previous and following bunch-crossings. Reconstructed events are reweighted to reproduce the measured distributions of the number of simultaneous interactions in different data-taking periods and the measured effects of various sources of reconstruction inefficiencies, for example in the application of electron identification algorithms. Specific kinematic variables, such as lepton momenta, are smeared to reproduced measured detector resolution.

The MC generators used to simulate the various SM processes of interest are summarised in Table 1 for the main processes, together with the selected parton shower algorithms, the sets of tuned parameters (tunes), and the sets of parton distribution functions (PDF). When PYTHIA is used, the decays of bottom and charm hadrons are simulated with the EVTGEN program [89]. Diboson processes [76] include all resonant and non-resonant $pp \to 4\ell/\ell^+\ell^-\nu\nu$ processes of order α^4 in the fine structure constant, including Higgs boson contributions, as well as the vector boson scattering/fusion processes $pp \to 4\ell/\ell^+\ell - \nu\nu jj$ at order α^6. Triboson processes similarly include all resonant and non-resonant $pp \to 6\ell/4\ell 2\nu/\ell^+\ell^- 4\nu$ processes at order α^6. The associated production of $t\bar{t}$ and a on-shell W boson includes a complementary sample generated at leading order (LO) in QCD with the matrix elements of order α^3. Associated production of $t\bar{t}$ and a pair of same-flavour opposite-sign (SFOS) leptons is generated down to a dilepton invariant mass of 1 GeV. Other processes not identified individually in the table but included in the background estimates

---

[2] Prompt leptons are defined are those produced neither in the decay of a hadron, nor radiatively in the fragmentation of quarks and gluons, nor in the material conversion of a photon of other origin than the electromagnetic shower of a charged lepton. They may originate from the leptonic decay of a prompt τ.

Process	Generator	Computation order	Parton shower	Cross-section normalisation	PDF set	Set of tuned parameters
$t\bar{t}W$ [62]	Sherpa 2.2.10 [63] + OpenLoops [66–68]	NLO 0-1j + LO 2j + LO $\mathcal{O}(\alpha^3\alpha_S)$	CSShower [64]	NLO	NNPDF3.0nlo [65]	default
$t\bar{t}\ell^+\ell^-$ [62]	Sherpa 2.2.1 [63]	NLO	CSShower [64, 69]	NLO	NNPDF3.0nlo [65]	default
$1 < m_{\ell\ell} < 5$ GeV	MG5_aMC@NLO 2.3.3 [3]	NLO	Pythia 8.212 [70]	NLO	NNPDF3.0nlo [65]	A14 [71]
$t\bar{t}H$ [72]	Powheg Box v2 [63]	NLO	Pythia 8.230 [70]	NLO [73]	NNPDF3.0nlo [65]	A14 [71]
$t\bar{t}t\bar{t}$ [62]	MG5_aMC@NLO 2.3.3 [3] + MadSpin [74, 75]	NLO	Pythia 8.230 [70]	NLO	NNPDF3.1nlo [65]	A14 [71]
other $t/t\bar{t} + X$ [62]	MG5_aMC@NLO 2.3.3 [3]	NLO or LO	Pythia 8.210-230 [70]	NLO or LO	NNPDF3.0/3.1nlo [65]	A14 [71]
diboson [76]	Sherpa 2.2.2 [63] + OpenLoops [66–68]	NLO 0-1j + LO 2-3j	CSShower [64, 69]	NLO	NNPDF3.0nnlo [65]	default
triboson [76]	Sherpa 2.2.1 [63]	LO 0-1j	CSShower [64, 69]	NLO	NNPDF3.0nnlo [65]	default
$t\bar{t}$ [77]	Powheg Box v2 [78–81]	NLO	Pythia 8.230 [82]	NNLO [77]	NNPDF3.0nlo [65]	A14 [71]
single top (s, t)	Powheg Box v2 [79–81, 83]	NLO	Pythia 8.230 [82]	NNLO [84, 85]	NNPDF3.0nlo [65]	A14 [71]
(tW)	Sherpa 2.2.7 [63]	NLO	CSShower [64, 69]	NNLO + NNLL [86]	NNPDF3.0nnlo [65]	default
$W \to \ell\nu, Z/\gamma^* \to \ell\ell$ [87]	Sherpa 2.2.11 [63]	NLO 0-2j + LO 3-4j	CSShower [64, 69]	NNLO [87, 88]	NNPDF3.0nnlo [65]	default

Table 1: List of Monte Carlo event generators and their settings for the main simulated samples of SM processes. When no reference is provided for the cross-section normalisation, the one computed by the generator is used. The LO and NLO acronyms stand for leading-order and next-to-leading-order calculations, respectively; in some cases (indicated), matrix elements are used with different accuracies depending on the number of additional parton emissions.

comprise the associated production of $t\bar{t}$ and two vector or Higgs bosons, the associated production of single top quarks with one or two vector or Higgs bosons, and the production of three top quarks. Fast detector simulation is employed for the following processes: $4t$, tH, tWH, $t\bar{t}ZZ$, $t\bar{t}WH$, $t\bar{t}HH$.

The SUSY signal samples are generated with MG5_aMC@NLO 2.6.2 [3] and the NNPDF2.3lo PDF, except for the $\tilde{g} \to q\bar{q}WZ\tilde{\chi}_1^0$ and $\tilde{g} \to t\bar{b}\bar{q}$ samples for which the NNPDF3.0lo PDF is used. The pair production of gluinos and squarks is simulated at LO complemented by matrix elements for up to two extra parton emissions. Superpartners not involved in the model of interest are decoupled by being assigned unreachable masses. The decays of gluinos or squarks are factored out of the hard interaction and simulated with Pythia 8.235 [82], which is also used for the subsequent stages of the event generation with the A14 tune [71]. The matching between matrix elements and parton shower is done following the CKKW-L prescription [90], with a matching scale set to one quarter of the gluino or squark mass. For all models, the fast simulation is used to process the generated events. Signal cross sections are calculated to approximate next-to-next-to-leading order in the strong coupling constant, adding the resummation of soft gluon emission at next-to-next-to-leading-logarithmic accuracy (approximate NNLO+NNLL) [91–98]. The nominal cross section and the uncertainty are derived using the PDF4LHC15_mc PDF set, following the recommendations of Ref. [99].

5 Object selection

Charged-particle tracks in the ID are reconstructed [100–102] up to $|\eta| = 2.5$ using recorded hits and environmental information (e.g. magnetic field, beam spot). Those satisfying $p_T > 500$ MeV and minimal quality criteria are associated to form primary vertices [103–105]. The reconstructed vertex with the largest $\sum p_T^2$ (the sum of its associated tracks' squared p_T) is assumed to be the position of the hard scattering interaction of interest. Events are not considered when such a vertex with at least two tracks is not found. Impact parameters [106] of tracks at their perigee with respect to this primary vertex are used to separate tracks originating from the hard scatter interaction, from those coming from pile-up or secondary interactions such as displaced hadron decays or photon conversions. The main variables used in the analysis are the longitudinal impact parameter $|z_0 \sin(\theta)|$, where the sine term dampens the effect of reduced accuracy in the forward region, as well as the ratio $|d_0^{\mathrm{sig}}|$ of the transverse impact parameter d_0 to its estimated uncertainty $\sigma(d_0)$. The directional component of reconstructed lepton four-momenta is also evaluated at their track's perigee.

Jets are reconstructed up to $|\eta| = 4.5$ with the FastJet implementation [107] of the anti-k_t algorithm [108] with radius parameter $R = 0.4$, out of particle-flow objects [109, 110] combining calorimeter energy deposits [111] and ID tracks. Jet p_{T}, energy and mass are then calibrated to the particle level [109], and only jets with $p_{\mathrm{T}} > 20\,\mathrm{GeV}$ are retained. The analysis ignores jets originating from pile-up interactions according to a track-based discriminant [112]. For the selection criteria referring to a number of jets, only jets with $|\eta| < 2.8$ are counted. Finally, about 0.5% of selected events, believed to contain jets from other sources [113] than the pp interactions, are also entirely discarded.

Within the ID acceptance, jets containing bottom hadrons (referred to as b-jets) are identified with the DL1r tagging algorithm [114], a deep neural network combining information from lower-level MVA discriminants exploiting the topology of reconstructed tracks and secondary vertices. The analysis selects b-jets with an estimated 70% efficiency in $t\bar{t}$ events while rejecting 99.8% of other jets free of charm hadrons or taus [114].

Muons within $|\eta| < 2.5$ and satisfying $p_{\mathrm{T}} > 10\,\mathrm{GeV}$ are used. They are provided [115] by an iterated track fit of ID and MS hits accounting for ionisation losses in the calorimeters, and seeded either by matched pairs of independently-reconstructed ID and MS tracks, or by a set of MS hits found along the extrapolated trajectory of an ID track. Momentum corrections [116] compensate for residual detector misalignments. The `Medium` quality criteria defined in Ref. [115] are applied, and pile-up muons are rejected by requiring $|z_0 \sin(\theta)| < 0.5\,\mathrm{mm}$. The candidates satisfying these requirements are called in the following baseline muons. About 0.1% of selected events are rejected as they contain either a muon from likely cosmic origin, or a muon with poor expected momentum resolution. Prompt muons are then distinguished from background sources by requiring $|d_0^{\mathrm{sig}}| < 3$ and isolation [115, 117] from other final state products. The latter requirement consists in an upper bound on the summed $|p_{\mathrm{T}}|$ of suitable ID tracks[3] within $\Delta R < \min(30\,\mathrm{GeV}, \text{muon } p_{\mathrm{T}})/10\,\mathrm{GeV}$, set to 6% of the muon p_{T}. The candidates satisfying all selection criteria are referred to as signal muons.

Similarly, electrons within $|\eta| < 2.47$ and satisfying $p_{\mathrm{T}} > 10\,\mathrm{GeV}$ are used. They are reconstructed [117] from clustered energy deposits in the electromagnetic calorimeter matched to an ID track, the latter being subsequently refitted to account for bremsstrahlung losses inherent to electron trajectories. A momentum calibration procedure [117, 118] based on boosted decision trees (BDTs) allows to correct the measured energy for various losses, e.g. in passive upstream material such as the calorimeter enclosure or the solenoid magnet. Electrons within the transition region $1.37 < |\eta| < 1.52$ between the barrel and endcap calorimeters are not considered. A first set of requirements aimed at rejecting the majority of background sources is applied, primarily based on a likelihood discriminant [117] built from topological information on the development of the electron shower in the calorimeter, its compatibility with the matched track, and particle identification capability of the TRT detector. Electrons with $|z_0 \sin(\theta)| > 0.5\,\mathrm{mm}$ are rejected. The candidates satisfying these requirements are called in the following baseline electrons. Non-prompt or fake electron sources are then further suppressed by keeping only electrons within $|\eta| < 2.0$, imposing the tighter `MediumLH` identification criteria [117], requiring $|d_0^{\mathrm{sig}}| < 5$, and a combination of track-based and calorimeter isolation. Track-based isolation is very similar to the muon isolation described above, with

---

[3] those with $p_{\mathrm{T}} > 1\,\mathrm{GeV}$, originating from the primary vertex, excluding the muon's own track; more details can be found in the references.

the addition that tracks within $|\Delta\eta| < 0.01$ of the electron track are also ignored. Calorimeter isolation is detailed in Ref. [117] and may be summarized as a 6% upper bound on pure calorimeter activity within a $\Delta R < 0.2$ cone around the electron with respect to its p_{T} and excluding a simple estimate of its own contribution, together with corrections for pile-up. Finally, the rate of wrong charge assignment amongst surviving electron candidates is further reduced by an order of magnitude by rejecting electrons likely to have a wrong charge according to the `ECIDS` discriminant [117], a BDT based on the properties of the electron track which accepts close to 98% of simulated $Z \to ee$ electrons. The candidates satisfying all selection criteria are referred to as signal electrons.

Different types of objects might be reconstructed independently out of the same detector information, as the optimal choice for preferring one type of object over another may be context-dependent. An overlap removal procedure is therefore applied to baseline lepton candidates and jets. Jets close to electrons ($\Delta R < 0.2$) are ignored, unless they are classified as b-jets with $p_{\mathrm{T}} < 100$ GeV. Those close to muons ($\Delta R < 0.2$ or sharing an ID track) are also ignored if they have less than 3 associated ID tracks, which marks them as likely muon bremsstrahlung. Leptons close to remaining jets ($\Delta R < \min(0.4, 0.1 + 9.6\,\mathrm{GeV}/p_{\mathrm{T}}(\ell))$) are ignored, as likely to be fake or non-prompt; the ΔR threshold is smaller at high p_{T} to preserve lepton selection efficiency e.g. in boosted top quark decays or boosted $\tilde{\chi}_1^0$ decays (Figure 1(e)). Leftover electrons close to muons ($\Delta R < 0.01$) or to higher-p_{T} electrons ($\Delta R < 0.05$) are ignored. In the whole procedure, ΔR is calculated with the rapidity y rather than the pseudorapidity η.

The missing transverse momentum $\mathbf{p}_{\mathrm{T}}^{\mathrm{miss}}$ and its magnitude $E_{\mathrm{T}}^{\mathrm{miss}}$ are reconstructed [119] from selected electrons, muons and jets prior to overlap removal, together with reconstructed photons ($p_{\mathrm{T}} > 25$ GeV, $|\eta| < 2.37$) satisfying `Tight` identification criteria [117] and a track-based term gathering softer contributions not included in aforementioned objects. The $E_{\mathrm{T}}^{\mathrm{miss}}$ reconstruction employs its own overlap removal procedure.

6 Event selection

Events with $E_{\mathrm{T}}^{\mathrm{miss}} < 250$ GeV were selected using dilepton triggers [120, 121]. The lepton p_{T} thresholds varied throughout the full data-taking period up to a maximum of 24 GeV for triggers requiring two electrons, 22 GeV for triggers requiring two muons, and 17 GeV (14 GeV) for the electron (muon) in different-flavour dilepton triggers. For events with $E_{\mathrm{T}}^{\mathrm{miss}} > 250$ GeV, a logical OR of these triggers and $E_{\mathrm{T}}^{\mathrm{miss}}$ triggers [122] was used. Events are preselected by requiring exactly two signal leptons with the same electric charge or at least three signal leptons[4] without any charge requirement.

Multiple signal regions (SRs) have been defined with the goal of maximising the sensitivity to the signal models shown in Figure 1. Those SRs are not exclusive and can overlap. They are primarily built on the requirement of the number of signal ($n_{\mathrm{Sig}}(\ell)$) and/or baseline ($n_{\mathrm{BL}}(\ell)$) leptons and their relative charges, the number of b-jets ($n_{b\text{-jets}}$) with $p_{\mathrm{T}} > 20$ GeV, the number of jets (n_{jets}) with p_{T} above 25, 40 or 50 GeV, regardless of their flavour, and apply selections independently to a series of observables sensitive to the differences in kinematics between signal and background. One of the most relevant observables used across all SRs is the effective mass, m_{eff}, which aids in establishing the mass scale of the processes being probed, and is defined as the scalar sum of the p_{T} of jets, leptons, and $E_{\mathrm{T}}^{\mathrm{miss}}$ of the event,

$$m_{\mathrm{eff}} = \sum p_{\mathrm{T}}^{\mathrm{jet}} + \sum p_{\mathrm{T}}^{\ell} + E_{\mathrm{T}}^{\mathrm{miss}}. \qquad (1)$$

---

[4] In the following, unless otherwise stated, leptons refer to signal leptons.

6.1 RPC SRs

SRs targeting the RPC models are shown in Tables 2-5. Depending on the model, RPC SRs can require events with at least two leptons with the same electric charge, or three or more leptons. SRs with a three lepton selection accept any charge combination for the three leptons. A veto on b-tagged jets is imposed in order to reduce SM backgrounds with top quarks. For those signal models not involving the presence of a Z-boson in the final state (Figures 1(c) and 1(d)), events in which the invariant mass of any pair of two same-flavour opposite-sign leptons is compatible with the Z-boson mass are vetoed ($m_{\text{SFOS}} \notin [81, 101]$ GeV).

SRs targeting the benchmark models of the cascade decays of charginos into pairs of SM bosons originating from the pair production of gluinos (Figure 1(a)) and squarks (Figure 1(b)) are named SRGGWZ and SRSSWZ, respectively. Multiple SRs are defined for every benchmark model, specifically tailored to target the different neutralino and gluino (squark) mass splitting scenarios. Those different scenarios are identified by the suffix '-L', '-M', and '-H' in the SR name, with 'H' being the scenario where $m_{\tilde{g}(\tilde{q})} \gg m_{\tilde{\chi}_1^0}$, 'L' denoting the scenario where $m_{\tilde{g}(\tilde{q})} \approx m_{\tilde{\chi}_1^0}$, and 'M' referring to the SR defined for the intermediate phase space between 'L' and 'H'. For those benchmark models where squarks are pair produced, the SR '-M' is further split into a region in the intermediate phase space close to the low mass splitting, '-ML', and another one close to the high mass splitting, '-MH'. Requirements on the jet multiplicity, $E_{\text{T}}^{\text{miss}}$, m_{eff} or $\sum p_{\text{T}}^{\text{jet}}$, are placed depending on the kinematics of the objects generated at the different mass splitting scenarios. Additional selection criteria are applied to other observables that were found to provide a good discrimination between the signal and the background. Those variables are the ratios between the different terms present in Equation 1, i.e. $E_{\text{T}}^{\text{miss}}/\sum p_{\text{T}}^{\text{jet}}$, $E_{\text{T}}^{\text{miss}}/m_{\text{eff}}$, $E_{\text{T}}^{\text{miss}}/\sum p_{\text{T}}^{\ell}$, $m_{\text{eff}}/\sum p_{\text{T}}^{\ell}$, $\sum p_{\text{T}}^{\ell}/\sum p_{\text{T}}^{\text{jet}}$; the azimuthal separation between the system formed by the two leading leptons and the direction of the missing transverse momentum of the event, $\Delta\phi(\ell 1 \ell 2, \mathbf{p}_{\text{T}}^{\text{miss}})$; and the $E_{\text{T}}^{\text{miss}}$ significance, Sig($E_{\text{T}}^{\text{miss}}$) [123].

SR name	$n_{\text{Sig}}(\ell)$ ($n_{\text{BL}}(\ell)$)	$n_{b\text{-jets}}$	n_{jets}	$p_{\text{T}}^{\text{jet}}$ [GeV]	$E_{\text{T}}^{\text{miss}}$ [GeV]	m_{eff} [GeV]	$\Delta\phi(\ell 1 \ell 2, \mathbf{p}_{\text{T}}^{\text{miss}})$	Sig($E_{\text{T}}^{\text{miss}}$)
SRGGWZ-L	≥ 2 (≥ 3)	0	≥ 6	> 25	> 200	$> 8 \times \sum p_{\text{T}}^{\ell}$	> 0.2	> 6
SRGGWZ-M	≥ 2 (–)		≥ 6	> 40	> 190	> 1300	> 0.8	–
SRGGWZ-H	≥ 2 (–)		≥ 6	> 40	> 150	> 2100	–	–

Table 2: Definition of the signal regions used for the RPC model shown in Figure 1(a), with the cascade decays of charginos into pairs of SM bosons originating from the pair production of gluinos.

SR name	$n_{\text{Sig}}(\ell)$	$n_{b\text{-jets}}$	n_{jets}	$p_{\text{T}}^{\text{jet}}$ [GeV]	$E_{\text{T}}^{\text{miss}}$ [GeV]	m_{eff} [GeV]	$E_{\text{T}}^{\text{miss}}/\sum p_{\text{T}}^{\ell}$	$\sum p_{\text{T}}^{\ell}/\sum p_{\text{T}}^{\text{jet}}$	$n_{Z\to\ell^+\ell^-}$
SRSSWZ-L	≥ 3	0	≥ 4	> 25	$> 0.2 \times m_{\text{eff}}$	–	–	< 0.2	$0^{\dagger}$
SRSSWZ-ML			≥ 6	> 25	> 150	> 800	> 1.2	< 0.3	$\geq 1^{\dagger}$
SRSSWZ-MH			≥ 5	> 40	> 200	> 900	> 1.1	< 0.4	$\geq 1^{\dagger}$
SRSSWZ-H			≥ 5	> 40	> 250	> 1500	> 0.3	< 0.7	–

†: based on number of SFOS pairs with $81 < m_{\text{SFOS}} < 101$ GeV

Table 3: Definition of the signal regions used for the RPC model shown in Figure 1(b), with the cascade decays of charginos into pairs of SM bosons originating from the pair production of squarks.

SRs targeting the benchmark models of decays of charginos and neutralinos into sleptons originating from the pair production of gluinos (Figure 1(c)) and squarks (Figure 1(d)) are named SRGGSlep and SRSSSlep, respectively. Multiple SRs are defined for the different mass splitting scenarios and named as per the convention described previously. An extra SR (SRSSSlep-H (loose)) is defined for the RPC model shown in Figure 1(d), using the same selection criteria as for SRSSSlep-H, but with the m_{eff} requirement relaxed to 1 TeV to allow for a binned fit in the model dependent interpretation. SRs are defined in terms of the variables previously described, with requirements also placed on the p_{T} of the leading and sub-leading lepton, denoted as $p_{\text{T}}^{\ell 1}$ and $p_{\text{T}}^{\ell 2}$, respectively; and on the angular distance between the two leading leptons, $\Delta R(\ell 1, \ell 2)$.

SR name	$n_{\text{Sig}}(\ell)$	$n_{b\text{-jets}}$	n_{jets}	$p_{\text{T}}^{\text{jet}}$ [GeV]	$E_{\text{T}}^{\text{miss}}$ [GeV]	$E_{\text{T}}^{\text{miss}}/\sum p_{\text{T}}^{\text{jet}}$	$p_{\text{T}}^{\ell 2}$ [GeV]	other
SRGGSlep-L	$\geq 3^{\dagger}$	0	≥ 4	≥ 40	–	> 0.4	> 30	$E_{\text{T}}^{\text{miss}}/\sum p_{\text{T}}^{\ell} > 1.4$
SRGGSlep-M					> 150	> 0.3	> 70	$\Delta\phi(\ell 1 \ell 2, \mathbf{p}_{\text{T}}^{\text{miss}}) > 0.7$
SRGGSlep-H					> 100	–	–	$\sum p_{\text{T}}^{\text{jet}} > 1200$ GeV
†: SFOS pairs with $81 < m_{\text{SFOS}} < 101$ GeV are not allowed								

Table 4: Definition of the signal regions used for the RPC model shown in Figure 1(c), for the decays of charginos and neutralinos into sleptons originating from the pair production of gluinos.

SR name	$n_{\text{Sig}}(\ell)$	p_{T}^{ℓ} [GeV]	$n_{b\text{-jets}}$	n_{jets}	$p_{\text{T}}^{\text{jet}}$ [GeV]	$E_{\text{T}}^{\text{miss}}$ [GeV]	m_{eff} [GeV]	$\Delta\phi(\ell 1 \ell 2, \mathbf{p}_{\text{T}}^{\text{miss}})$
	other requirements							
SRSSSlep-L	3^{*}	< 60	0	≥ 3	$> 60, 60, 25$	> 100	> 600	> 1.4
	$\sum p_{\text{T}}^{\ell}/\sum p_{\text{T}}^{\text{jet}} < 0.6$							
SRSSSlep-ML	3^{*}	> 30	0	≥ 3	$> 60, 60, 25$	> 100	> 700	> 1.4
	$E_{\text{T}}^{\text{miss}}/\sum p_{\text{T}}^{\ell} > 0.7$, $\sum p_{\text{T}}^{\ell}/\sum p_{\text{T}}^{\text{jet}} < 0.6$							
SRSSSlep-MH	3^{*}	> 40	0	≥ 2	> 60	> 200	> 1000	> 0.5
	$E_{\text{T}}^{\text{miss}}/\sum p_{\text{T}}^{\ell} > 0.7$, $\Delta R(\ell 1, \ell 2) > 0.2$							
SRSSSlep-H	3^{*}	> 40	0	≥ 2	> 60	> 200	> 2000	> 0.3
	$\Delta R(\ell 1, \ell 2) > 0.5$							
SRSSSlep-H (loose)	3^{*}	> 40	0	≥ 2	> 60	> 200	> 1000	> 0.3
	$\Delta R(\ell 1, \ell 2) > 0.5$							
*: additional baseline leptons are not allowed, nor SFOS pairs with $81 < m_{\text{SFOS}} < 101$ GeV								

Table 5: Definition of the signal regions used for the RPC model shown in Figure 1(d), for the decays of charginos and neutralinos into sleptons originating from the pair production of squarks. Requirements on p_{T}^{ℓ} apply to all three leptons.

6.2 RPV SRs

SRs targeting the RPV models are shown in Tables 6 and 7. The SRs are named SRLQD and SRUDD, where the former corresponds to the SR defined for the model where the neutralino decays via the λ' RPV coupling of LQD type (Figure 1(e)), and the latter to the SRs defined for the model where gluinos decay via top squarks and the λ'' RPV coupling of UDD type (Figure 1(f)). For this last one, the suffix in the SR name indicates the requirement on the number of b-jets. Those SRs require exactly two leptons with the same electric charge, high jet multiplicity, and high $\sum p_{\text{T}}^{\text{jet}}$ or high m_{eff}. No requirement is applied on the $E_{\text{T}}^{\text{miss}}$ as no neutralinos are expected in the final state of RPV models.

SR name	$n_{\text{Sig}}(\ell)$	$n_{b\text{-jets}}$	n_{jets}	$p_{\text{T}}^{\text{jet}}$ [GeV]	m_{eff} [GeV]
SRLQD	2	–	≥ 5	> 50	> 2600

Table 6: Definition of the signal region used for the RPV model shown in Figure 1(e), where the neutralino decays via the λ' RPV coupling of LQD type.

SR name	$n_{\text{Sig}}(\ell)$	$n_{b\text{-jets}}$	n_{jets}	$p_{\text{T}}^{\text{jet}}$ [GeV]	m_{eff} [GeV]	$\sum p_{\text{T}}^{\text{jet}}$ [GeV]
SRUDD-1b	2	1	≥ 6	> 50	–	> 1600
SRUDD-2b		2	≥ 2	> 25	–	> 1700
SRUDD-ge2b		≥ 2	≥ 5	> 50	–	> 1600
SRUDD-ge3b		≥ 3	≥ 4	> 50	> 1600	–

Table 7: Definition of the signal regions used by the RPV model shown in Figure 1(f), where gluinos decay via top squarks and the λ'' RPV coupling of UDD type.

7 Background estimation

Different methods are employed to predict contributions to the regions of interest from SM processes with genuine same-sign leptons final states, and from other processes forming same-sign lepton pairs due to the presence of fake or non-prompt (F/NP) leptons or the incorrect reconstruction of the charge of an electron. The first type of background is estimated with MC simulations aided by a single control region in the data. For the other two, methods exploiting data events with specific lepton selection criteria are employed. A description of the methods for each of the backgrounds is given in the following three sections. Comparisons of background predictions to observed data in selected validation regions are presented in a fourth section.

7.1 SM processes with prompt same-sign leptons

The largest contribution to the RPC SRs originates from WZ + jets with both bosons decaying to leptons. All these SRs veto the presence of b-jets, which suppresses processes involving top quarks. For WZ + jets, a control region intermediate in jet multiplicity is employed, referred to as CRWZ2j. It is defined with three signal leptons (and no fourth baseline lepton), two of them forming a SFOS pair with invariant mass in the range $81 < m_{\text{SFOS}} < 101$ GeV. The two same-sign leptons of the triplet must have $p_{\text{T}} > 15$ GeV, and the sum of the three leptons p_{T} must be greater than 130 GeV. Events must contain either two or three jets ($p_{\text{T}} > 25$ GeV), with no b-jet present. Contributions from hypothetical BSM processes are reduced by requiring $30 < E_{\text{T}}^{\text{miss}} < 150$ GeV and $m_{\text{eff}} < 1.5$ TeV. This selection results in an estimated purity exceeding 85%, with the remainder dominated by other multiboson process. The overall normalisation of the WZ + jets MC prediction is then treated as a free parameter and set by fitting simultaneously the observed data yields in CRWZ2j and the relevant RPC SR. It is found that a scale factor of 0.84 ± 0.05 with respect to the MC prediction using the theoretical inclusive NLO cross section best accommodates the observed data in CRWZ2j. This below-unity value is consistent with past observations [124, 125]. In the RPV SRs, no simultaneous fit is performed and the WZ + jets normalisation is determined by the CRWZ2j alone. This sequential approach neglects the propagation of correlations in the WZ + jets uncertainties for RPV SRs, which does not affect the results as the WZ + jets background is subdominant in those SRs.

Other SM background processes with prompt same-sign leptons are simply estimated by normalising the simulated samples with the theoretical cross-section. Some rarer sources of same-sign leptons are ignored. Those include radiative top quark decays $t \to b\ell^+\nu\ell^+\ell^-$ in $t\bar{t}$ events, found to be minor in the context of Refs. [25, 126], or multiple parton scattering for which similar conclusions were reached in Ref. [25].

7.2 Electrons with incorrect charge

The electron reconstruction algorithm [117] determines the sign of the charge of the electron based on the curvature of its ID track. In the cases where the electron starts radiating early in the ID, the wrong charge may be assigned to it by the algorithm. This situation is referred to as charge flip in the following. It results in a small production of same-sign ee or $e\mu$ pairs from processes such as $Z \to \ell^+\ell^-$ or $t\bar{t} \to bb\ell^+\ell^-\nu\bar{\nu}$. As indicated in Section 5, the dedicated `ECIDS` BDT is employed as part of the signal electron selection to identify and reject such cases. The residual probability for signal electrons to exhibit a charge flip is around 0.06% in the validation region with the largest charge-flip contribution. It varies by several orders of magnitude with $|\eta|$ and p_{T} as illustrated in Ref. [117].

Contributions from charge flip background to regions of interest of the analysis are estimated by selecting data events with opposite-sign rather than same-sign leptons and weighting them according to the known charge flip probabilities. The latter are calculated in simulated $t\bar{t}$ events, and are themselves corrected to data by an analysis-independent calibration [117] exploiting the charges of observed dielectron pairs at the $\mathrm{Z} \to ee$ resonance; those corrections factors are found to be within 20% of unity. The probabilities and the corrections are both measured as function of $|\eta|$ and p_{T}. Despite the momentum scale and resolution of charge flip electrons being known to differ from those of regular electrons, no momentum correction of the opposite-sign pairs is made, on the basis that previous analyses [25] found the impact of this effect negligible. A complementary set of probabilities is also calculated for the loosely-selected electrons used for the fake lepton background estimate; indeed, the charge flip probability can be an order of magnitude higher for candidates that fail signal electron requirements. In this case, the corrections to data are assumed to be the same as for signal electrons.

The dominant uncertainties in the predicted charge flip yields are those arising from the measurement of the correction factors [117], which is statistically limited and affected by a significant background. The predicted yields suffer from a typical uncertainty of 50%, which however does not impact significantly the results of the present analysis since they represent at most 7% of the total background in any of the SRs.

7.3 Fake and non-prompt leptons

Non-prompt leptons arising from hadron decays or photon conversions, as well as hadrons misreconstructed as electrons, may survive with a low rate the identification criteria of Section 5. Combined with the presence of a prompt lepton in the event, a same-sign lepton pair may be formed. This source of background is estimated primarily with the matrix method summarised in the following paragraphs, whose prediction is then compared to that of a corrected simulation [54, 127].

The matrix method [128] exploits the different response of F/NP leptons to the identification and isolation requirements. In a given region of interest, data events are selected by applying looser lepton selection criteria than those defining signal leptons, and categorising those events depending on the number of actual signal leptons. A fully-determined system of linear equations can then be constructed, relating the numbers of such categorised events to the (unknown) numbers of events with only prompt leptons / exactly one F/NP lepton / etc, where coefficients are functions of the probabilities ε, ζ for loose prompt or F/NP leptons to also satisfy the nominal criteria. This can be illustrated for events with a single lepton by the following:

$$\begin{pmatrix} n_{\text{signal}} \\ n_{\text{all}} \end{pmatrix} = \begin{pmatrix} 1 & 1 \\ \frac{1}{\varepsilon} & \frac{1}{\zeta} \end{pmatrix} \cdot \begin{pmatrix} n_{\text{signal, prompt}} \\ n_{\text{signal, F/NP}} \end{pmatrix} \tag{2}$$

The desired estimate $n_{\text{signal, F/NP}}$ can then be obtained easily. The approach extends readily to final states with multiple leptons. The general method is described in detail in Ref. [129]; the present analysis relies upon the software implementation referrenced herein. The sample of loosely-selected leptons consists in the subset of baseline leptons after overlap removal which for muons satisfy $|d_0^{\text{sig}}| < 7$, and for electrons satisfy the `ECIDS` requirement and are restricted to $|\eta| < 2.0$. The estimated contribution of charge-flip electrons is subtracted from all the observables entering the equations, in order not to interfere with the estimate.

The probabilities ε and ζ have to be supplied. The former are calculated with simulated $t\bar{t}$ decays to leptons. The latter are measured in the range $10 < p_{\text{T}} < 75$ GeV in dedicated regions in data enriched predominantly in $t\bar{t}$ events with one or two prompt leptons and one F/NP lepton forming a same-sign pair, which is also the leading contributor of F/NP leptons to the SRs. The measurements are performed as a function of p_{T} and (for ε) $|\eta|$ of the lepton, as well as (for ζ) the number of b-jets in the event (≤ 1 or ≥ 2) and whether the electron satisfies the criteria [120] to trigger the event recording. More details can be found in Ref. [25]. The undesirable contributions of WZ+jets and $t\bar{t}W$ to those measurement regions, estimated with MC, are however now adjusted by correction factors of 0.84 and 1.19 respectively based on observed data in CRWZ2j and the region VRTTV defined in Table 8. For muons, ε is found to increase logarithmically with p_{T} from 75% at 10 GeV up to 98% at 70 GeV, while ζ varies between 10% and 15% in the most relevant range $10 < p_{\text{T}} < 40$ GeV reaching minimal values around 20 GeV. For electrons, ε also increases logarithmically with p_{T} from 50% at 10 GeV up to 97% at 100 GeV, while ζ varies between 5% and 10% in the aforementioned p_{T} range. When the electron satisfies the trigger criteria, ζ values can be up to twice larger. Over the whole measurement range and for both lepton flavours, ε is always found to be much larger than ζ, a necessary condition for the applicability of the matrix method [129]. The same conservative systematic uncertainties as detailed in Ref. [25] are used to account for contamination of prompt same-sign lepton processes in the measurement regions, and the assumption that ε and ζ can be used outside of the regions in which they are measured. In the SRGGWZ-L region, which only selects events containing a third baseline lepton in addition to the pair of same-sign signal leptons, the estimate is calculated with the reasonable assumption that the F/NP lepton is part of the latter pair.

The SR yields predicted with the matrix method were cross-checked against those predicted by MC simulations of $t\bar{t}$ and W/Z + jets processes. Simulated events with F/NP leptons are weighted by three correction factors extracted from fits on data in appropriate regions: one for F/NP electrons, one for non-prompt muons from bottom hadron decays, one for other sources of non-prompt muons. The estimates are compatible within uncertainties with the ones obtained with the matrix method.

7.4 Validation of the background estimates

In order to check the predictions of WZ + jets, $t\bar{t}W$ and $t\bar{t}\ell^+\ell^-$ reasonably close to the SRs, dedicated validation regions (VRs) are defined and presented in Table 8. The purity in the targeted SM process are expected to range from 70 to 80% for the two VRWZ regions, and 30 to 55% for the four VRTTV/VRTTW regions, while the expected contributions from SUSY signal processes remain small. The VRs are designed

	$n_{\mathrm{Sig}}(\ell)$	$n_{b\text{-jets}}$	n_{jets}	$p_{\mathrm{T}}^{\mathrm{jet}}$ [GeV]	m_{eff} [GeV]	$E_{\mathrm{T}}^{\mathrm{miss}}$ [GeV]
	other requirements					
VRWZ4j	3^*	0	≥ 4	> 25	$[600, 1500]$	$[30, 250]$
	$E_{\mathrm{T}}^{\mathrm{miss}}/m_{\mathrm{eff}} < 0.2$, $81 < m_{\mathrm{SFOS}} < 101$ GeV					
VRWZ6j	3^*	0	≥ 6	> 25	$[400, 1500]$	$[30, 250]$
	$E_{\mathrm{T}}^{\mathrm{miss}}/m_{\mathrm{eff}} < 0.15$, $81 < m_{\mathrm{SFOS}} < 101$ GeV					
VRTTV	≥ 2	≥ 1	≥ 3	> 40	$[600, 1500]$	$[30, 250]$
	$p_{\mathrm{T}} > 30$ GeV for the two leading-p_{T} same-sign leptons, $\Delta R > 1.1$ between the leading-p_{T} lepton and any jet, $\sum p_{\mathrm{T}}^{b\mathrm{-jet}}/\sum p_{\mathrm{T}}^{\mathrm{jet}} > 0.4$, $E_{\mathrm{T}}^{\mathrm{miss}}/m_{\mathrm{eff}} > 0.1$					
VRTTV1b6j	≥ 2	≥ 1	≥ 6	> 40	< 1500	$[30, 250]$
	$p_{\mathrm{T}} > 30$ GeV for the two leading-p_{T} same-sign leptons, $E_{\mathrm{T}}^{\mathrm{miss}}/m_{\mathrm{eff}} < 0.15$					
VRTTW	2^* $(\mu^{\pm}\mu^{\pm})$	≥ 2	≥ 2	> 25	< 1500	$[30, 250]$
	both leptons with $p_{\mathrm{T}} > 25$ GeV, one with $p_{\mathrm{T}} > 40$ GeV					
VRTTW3j	2^* $(e^{\pm}\mu^{\pm})$	≥ 2	≥ 3	> 25	< 1500	$[30, 250]$
	both leptons with $p_{\mathrm{T}} > 25$ GeV					

*: additional baseline leptons are not allowed

Table 8: The definitions of validation regions aimed at verifying the accuracy of the SM background prediction. Requirements are placed on signal leptons, jets, and some of the event-level variables defined in Section 6.

	CRWZ2j	VRWZ4j	VRWZ6j	VRTTV	VRTTV1b6j	VRTTW	VRTTW3j
Observed	2848	395	55	117	119	265	442
Total SM background	$(285 \pm 5) \cdot 10^1$	$(42 \pm 5) \cdot 10^1$	73 ± 13	105 ± 16	86 ± 20	$(25 \pm 6) \cdot 10^1$	$(41 \pm 8) \cdot 10^1$
WZ	$(237 \pm 14) \cdot 10^1$	$(31 \pm 4) \cdot 10^1$	44 ± 11	3.5 ± 1.4	0.7 ± 0.2	2.3 ± 0.8	2.6 ± 0.8
$ZZ, W^{\pm}W^{\pm}, VVV$	$(21 \pm 10) \cdot 10^1$	25 ± 13	5.1 ± 2.8	0.8 ± 0.3	< 0.5	0.6 ± 0.2	0.7 ± 0.3
$t\bar{t}W$	1.7 ± 0.3	< 0.5	< 0.2	27 ± 4	18 ± 4	92 ± 14	116 ± 20
$t\bar{t}Z$	41 ± 9	35 ± 7	11 ± 3	32 ± 5	9.9 ± 3.1	22 ± 4	35 ± 6
$t\bar{t}t\bar{t}$	< 0.1	< 0.1	< 0.1	2.1 ± 0.4	8 ± 4	5.7 ± 1.2	7.8 ± 1.8
Other SM processes	$(8 \pm 4) \cdot 10^1$	18 ± 9	3.7 ± 1.9	19 ± 10	16 ± 8	36 ± 18	50 ± 25
Fake/non-prompt	$(15 \pm 7) \cdot 10^1$	27 ± 12	10 ± 4	15 ± 9	28 ± 16	87 ± 56	$(12 \pm 6) \cdot 10^1$
Charge-flip	–	–	–	5.7 ± 2.2	4.2 ± 1.6	–	72 ± 31

Table 9: The number of observed data events and expected background contributions in the CRWZ2j and the VRs, after fit. Background categories shown as "–" denote that they cannot contribute to a given region. The displayed yields include all sources of statistical and systematic uncertainties. The individual uncertainties can be correlated or anticorrelated and therefore do not necessarily add up in quadrature.

to be orthogonal to the SRs, with the exception of VRWZ4j and VRWZ6j which partially overlap with four of the SRGGWZ and SRSSWZ regions. For any of those, the number of expected shared SM background events does not exceed 3% of the total number of events in the VR. The background predictions and the observed numbers of events in CRWZ2J and in the VRs are given in Table 9, and illustrated in Figure 2. The data and the background expectation in all VRs agree within uncertainties. The largest tension occurs in VRWZ6j, for which it was verified that the level of agreement does not further deteriorate as function of m_{eff} or $E_{\mathrm{T}}^{\mathrm{miss}}$.

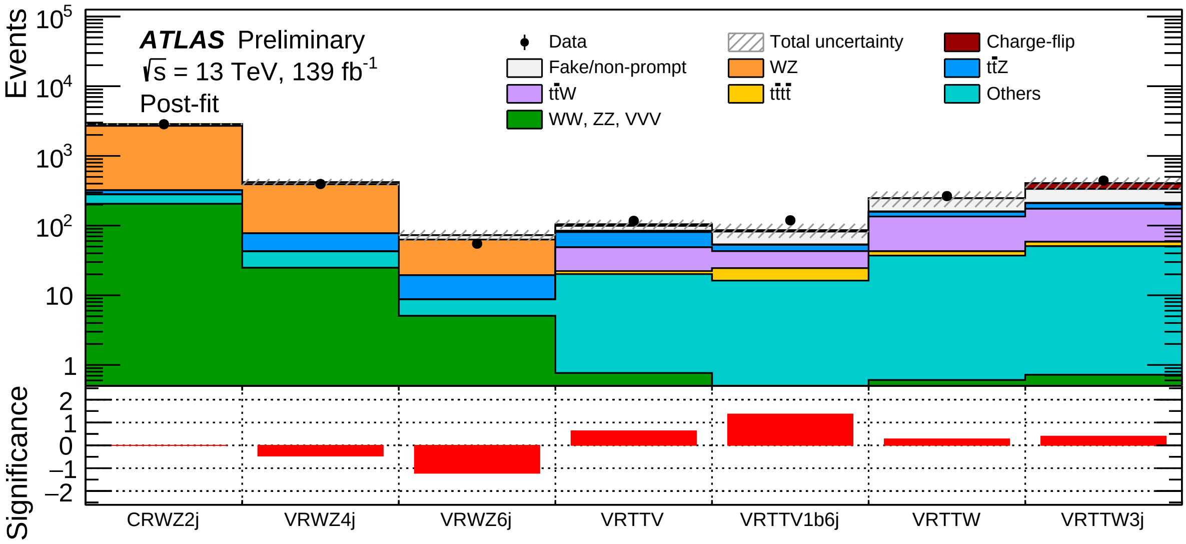

Figure 2: Data and post-fit background comparison in the CRWZ2j and the VRs. The bottom panel shows the significance quantifying the deviation of the observed yields from the background expectation. The total uncertainties in the expected event yields are shown as the dashed bands.

8 Systematic uncertainties

The predicted background yields in the SRs are affected by several sources of systematic and statistical uncertainties. The systematic uncertainties are grouped into experimental uncertainties, theoretical uncertainties, uncertainties from the data-driven methods described above, normalisation and MC statistical uncertainties.

The experimental uncertainties come from the possible differences between the data and simulations in elements used in this analysis and the uncertainties of the data taking of the operating detectors. They are related to luminosity, pileup, triggers, and the reconstructed objects. For luminosity, a 1.7% relative uncertainty [58] is applied. For pileup, the uncertainty is computed by performing a 4% up and down variation of the weights associated to $\langle\mu\rangle$. For leptons, uncertainties are computed for reconstruction efficiencies [117], identification efficiencies [115, 130], isolation efficiencies [131], energy scales [116, 117], resolutions, and trigger efficiencies [120–122] using varied methods. For jets, uncertainties are considered for jet vertex tagger (JVT) [132], jet energy scale (JES) [133] and jet energy resolution (JER) [109], and flavour tagging [134–136]. As for the $E_{\mathrm{T}}^{\mathrm{miss}}$, uncertainties are estimated by propagating the uncertainties in the energy and momentum scale of each of the objects entering the calculation, and the uncertainties in the soft term's resolution and scale [119].

The theoretical uncertainties comes from the MC modelling of the relevant SM and SUSY processes, including cross sections, choice of scales, the PDF and the α_s. The theoretical uncertainties from the dominant background processes in the signal regions like the WZ, $W^{\pm}W^{\pm}$, and the $t\bar{t}V$ (as well as $t\bar{t}t\bar{t}$ for RPV signal regions) are computed in detail. Uncertainties from the choice of renormalization scales, factorization scales, resummation scales, merging scales and the recoil schemes are considered and obtained by comparing the varied scales with the chosen scales. The impact of the choice of the PDF is evaluated by symmetrizing the event count variations with respect to the `MMHT2014` [137], `CT14` [138], and `NNPDF` [139]

PDF sets. For the remaining rarer processes mentioned in Table 1, an overall 50% uncertainty is assigned. The total cross section uncertainty is not applied to WZ process due to the normalisation of the WZ in the corresponding control regions according to the data.

For the purpose of defining correlations, the different processes are grouped into nine categories: WZ, $t\bar{t}W$, $t\bar{t}\ell\ell$, $t\bar{t}t\bar{t}$, other multiboson processes, other processes with top quarks, F/NP leptons, charge flip electrons, and SUSY signal. Within each group, all sources of uncertainties are treated as fully correlated, including across the different regions involved in the simultaneous fit. Experimental uncertainties are also treated as correlated between the different groups, while all other uncertainties are assumed to be uncorrelated. The total uncertainty and the separated contributions from each source are shown in Figure 3 and Figure 4 for CR/VRs and SRs separately. The total uncertainties vary from 1% (CRWZ2j) to 40% (SRUDD-1b). The dominant contributions are coming from the F/NP lepton background estimate, and the MC statistics in the SRs. The total uncertainty in the CRWZ2j is smaller than the individual components. It is caused by the anti-correlation between the normalisation and modelling uncertainties.

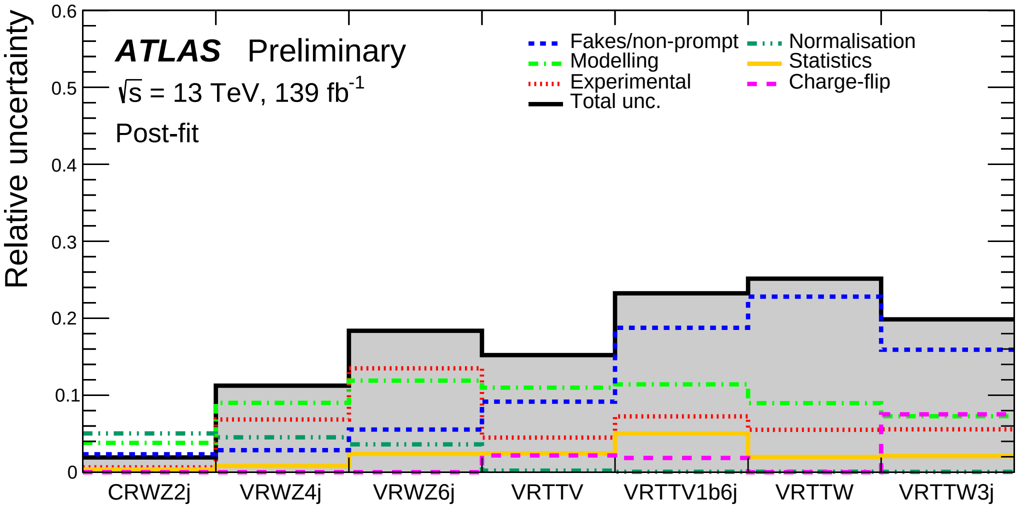

Figure 3: Relative contributions from different categories of the uncertainties in CRWZ2j and VRs. The correlation between the sources of the systematics are considered, therefore the total uncertainty do not necessarily match the quadrature summation of the individuals.

9 Statistical analysis

The expected SM backgrounds are determined with a profile likelihood fit [140], referred to as a background-only fit. The fit strategy differs between the RPC and RPV searches. For the RPC searches, the background-only fit uses the observed event yield in the CRWZ2j as a constraint to adjust the normalisation of the WZ+jets background assuming that no signal is present. The inputs to the background-only fit include the number of events observed in the CRWZ2j, and the number of events predicted in the CRWZ2j and the concerned SR(s) for all background processes. They are both described by Poisson statistics. The systematic uncertainties are included in the fit as nuisance parameters. They are constrained by Gaussian distributions with widths corresponding to the sizes of the uncertainties and are treated as correlated, when

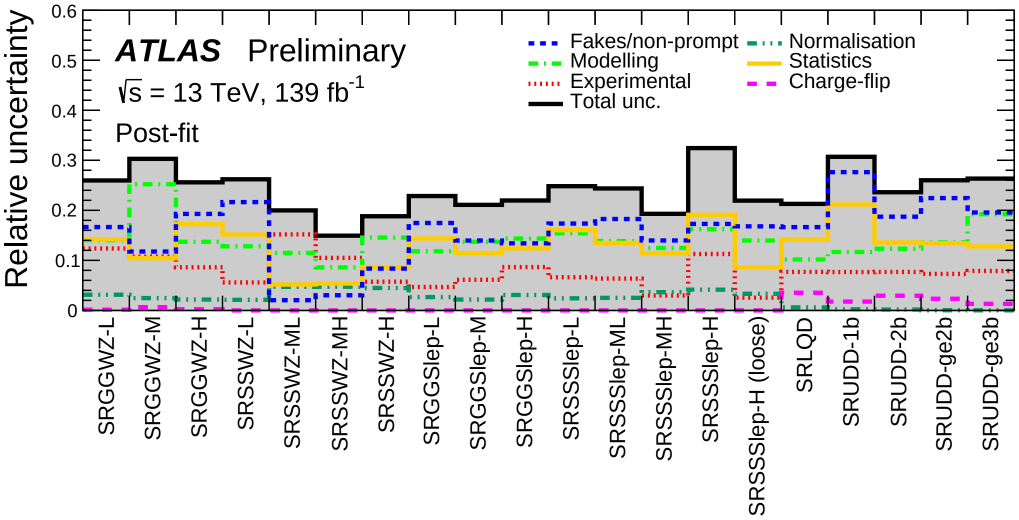

Figure 4: Relative contributions from different categories of the uncertainties in signal regions. The correlation between the sources of the systematics are considered, therefore the total uncertainty do not necessarily match the quadrature summation of the individuals.

appropriate, between the various regions. The product of the various probability density functions forms the likelihood, which the fit maximises by adjusting the normalisation of the WZ+jets background and the nuisance parameters. For the RPV searches, the CRWZ2j is not included in the fit, and the likelihood fit is used just to constrain the nuisance parameters associated with the systematic uncertainties. In both cases, the results of the background-only fit are used to test the compatibility of the observed data and the background estimates in the SRs.

In the absence of a significant excess over the SM expectation, two levels of interpretation are provided for BSM physics scenarios: model-independent exclusion limits and model-dependent exclusion limits set on the SUSY benchmark models illustrated in Figure 1. The $\mathrm{CL_s}$ method [141, 142] is used to derive the confidence level (CL) of the exclusion for a particular signal model. A signal model with a $\mathrm{CL_s}$ value below 0.05 is excluded at 95% CL.

Model-independent exclusion fits are used to set upper limits at 95% CL on the possible BSM contributions to the SRs. This fit proceeds in the same way as the background-only fit, with the CRWZ2j (for RPC searches) and SRs both participating in a simultaneous likelihood fit, and the likehood function accounting with an additional parameter-of-interest describing the potential signal contribution. Signal contamination in the CRWZ2j is assumed to be zero. The hypothesis tests are performed for each of the SRs independently. The limits have been evaluated using pseudo-experiments.

Model-dependent exclusion fits are used to set exclusion limits at 95% CL on the masses of gluinos and squarks for the SUSY benchmark models considered in this paper. The fit proceeds in a similar way as the model-independent fit, except that both the signal yield in the SRs and the signal contamination in the CRWZ2j are taken into account as predicted by the model, and the SRs are usually binned. Table 10 shows the SRs used for every benchmark model and the fitted observable in every SR. The observable providing the best sensitivity for every SR is chosen as the fitted variable. The binning of every observable has been optimised to provide the best sensitivity for the concerned benchmark model, while keeping enough statistics in every bin of the fitted SR. This multi-bin approach demonstrated to enhance the sensitivity for all the SUSY scenarios considered in this search. In this model-dependent fit, the $\mathrm{CL_s}$ is computed using the asymptotic approximation [143].

Model	Signal region(s)	Variable
$\tilde{g} \to qq'WZ\tilde{\chi}_1^0$ Fig. 1(a)	SRGGWZ-L || SRGGWZ-M || SRGGWZ-H	single-bin, m_{eff}, single-bin
$\tilde{q} \to q'WZ\tilde{\chi}_1^0$ Fig. 1(b)	SRSSWZ-L || SRSSWZ-ML || SRSSWZ-MH || SRSSWZ-H	$E_{\mathrm{T}}^{\mathrm{miss}}$, $E_{\mathrm{T}}^{\mathrm{miss}}$, m_{eff}, m_{eff}
$\tilde{g} \to q\bar{q}(\ell\ell/\nu\nu)\tilde{\chi}_1^0$ Fig. 1(c)	SRGGSlep-L || SRGGSlep-M || SRGGSlep-H	$E_{\mathrm{T}}^{\mathrm{miss}}/\sum p_{\mathrm{T}}^{\ell}$, $E_{\mathrm{T}}^{\mathrm{miss}}$, $E_{\mathrm{T}}^{\mathrm{miss}}$
$\tilde{q} \to q(\ell\nu/\ell\ell/\nu\nu)\tilde{\chi}_1^0$ Fig. 1(d)	SRSSSlep-L (loose) || SRSSSlep-ML || SRSSSlep-MH || SRSSSlep-H	m_{eff}
$\tilde{g} \to q\bar{q}\tilde{\chi}_1^0, \tilde{\chi}_1^0 \to \ell qq$ Fig. 1(e)	SRLQD	m_{eff}
$\tilde{g} \to \bar{\tilde{t}}t, \tilde{t} \to \bar{b}\bar{d}$ Fig. 1(f)	SRUDD-1b & SRUDD-ge2b	$\sum p_{\mathrm{T}}^{\mathrm{jet}}$

Table 10: Fit configuration used in order to obtain the exclusion limits for every benchmark model. The targeted signal model is shown in the first column. The second and third columns show the signal regions and the fitted variable in every signal region, respectively. The statistical combination of the signal regions is represented by the symbol "&" , while "||" means that for each point of the $\{m_{\tilde{g}(\tilde{q})}, m_{\tilde{\chi}_1^0}\}$ parameter space, the signal region with the best expected sensitivity is chosen.

10 Results

The observed number of events in each SR along with the background expectations and uncertainties are summarised in Figure 5, and detailed in Table 11. The background prediction corresponds to the estimation after the background-only fit described in Section 9. The overall excess (less than 2 standard deviations) observed in SRSSWZ-ML, SRSSWZ-MH, and SRSSWZ-H, is due to the overlap among these regions having three data events in common. Overlap among the remaining SRs is also observed, but in a smaller proportion. The contribution from WZ+jets dominates in the SRs with no b-jets, while the production of fake/non-prompt leptons and processes involving the top quark dominate in the SRs where the veto on b-jets is not applied. No significant excess of events above the SM prediction is observed in any of the SRs. The highest significance corresponds to SRSSslep-L with 2.3 standard deviations. The distributions of the most discriminant variable for some of the SRs, with the signal region requirement on the displayed variable removed, are shown in Figure 6.

In the absence of a significant deviation from the SM prediction, the results are interpreted in terms of model-independent upper limits on possible BSM contributions to the SRs, as well as exclusion limits on the masses of the SUSY particles of the benchmark scenarios shown in Figure 1. The 95% CL upper limits on the number of BSM events, S^{95}, that may contribute to the SRs are shown in Table 12. Normalising these by the integrated luminosity L of the data sample, they can be interpreted as upper limits on the visible BSM cross-section (σ_{vis}), defined as $\sigma_{\mathrm{vis}} = \sigma_{\mathrm{prod}} \times \mathcal{A} \times \epsilon = S^{95}/L$, where σ_{prod} is the production cross-section of an arbitrary BSM signal process, and $\mathcal{A}$ and ϵ are the corresponding acceptance and reconstruction efficiencies for the relevant SR. The probability of the observations being compatible with the SM-only hypothesis is quantified by the p-values displayed in the last column of Table 12. For SRs where the data yield is smaller than expected, the p-value is capped at 0.50.

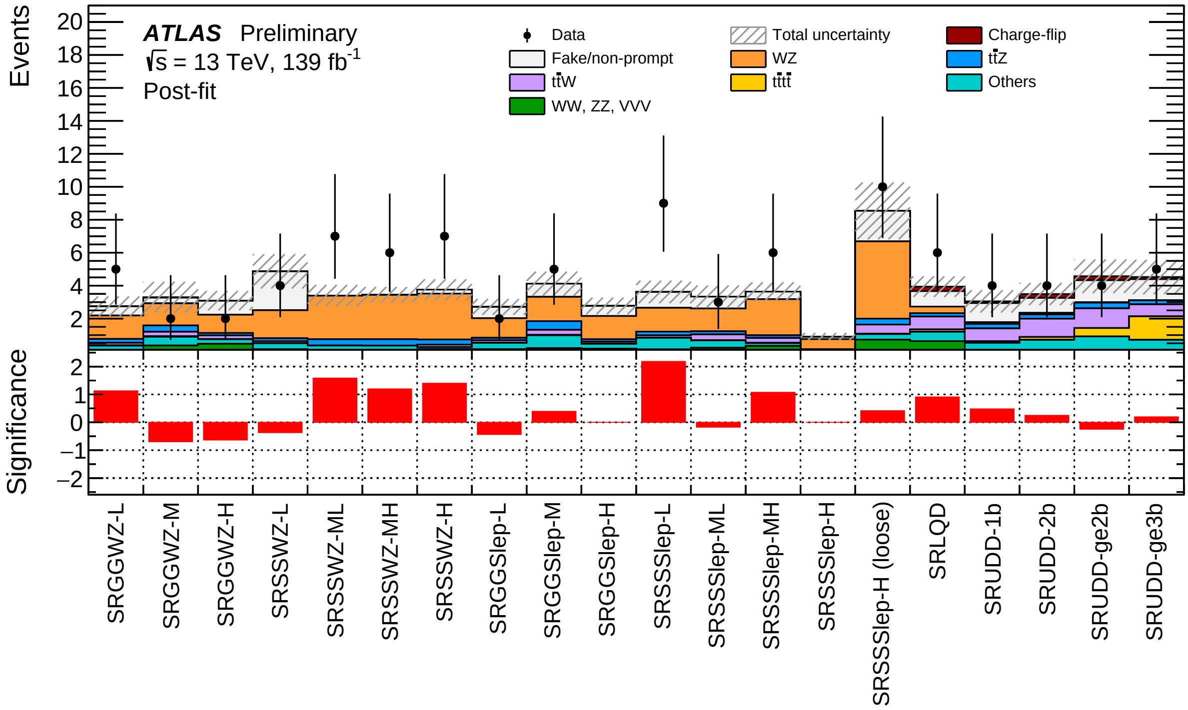

Figure 5: Data and post-fit background comparison in all SRs. The bottom panel shows the significance quantifying the deviation of the observed yields from the background expectation. The total uncertainties in the expected event yields are shown as the dashed bands.

Exclusion limits at 95% CL are also set on the masses of the superpartners involved in the SUSY benchmark scenarios considered. The area delimited by the SR in Figure 6 shows the fitted distribution for the displayed SR. The bins displayed above the SR requirement correspond to the binning used in the exclusion fit. For illustration purposes, only one SR per benchmark model is shown. Figure 7 shows the exclusion limits obtained for the RPC models shown in Figure 1. For each point of the $\{m_{\tilde{g}(\tilde{q})}, m_{\tilde{\chi}^0_1}\}$ parameter space, the SR with the best expected sensitivity is chosen. Figures 7(a) and 7(b) show the mass limits on gluinos and squarks, respectively, for the cascade decays of charginos into pairs of SM bosons. The mass limits on gluinos are up to 400 GeV higher than the previous limits, excluding gluinos with masses up to 2 TeV. For squarks, the mass limits improve by around 600 GeV with respect to the prior results, excluding squarks with masses up to 1.2 TeV.

Figures 7(c) and 7(d) show the mass limits on gluinos and squarks, respectively, for the decays of charginos and neutralinos into sleptons. The mass limits on gluinos are extended up to 2.2 TeV for a massless neutralino, while in the very compressed area, the limits on the neutralino mass improve by around 200 GeV the latest available results. For the model where squarks are pair produced, the mass limits on squarks are up to 850 GeV higher than the previous limits, excluding squarks with masses up to 1.7 TeV.

Figure 7(e) shows the mass limits on gluinos for the scenario where the neutralino decays via λ' RPV couplings. Gluinos with masses up to 2.2 TeV are excluded, extending considerably the results of the previous search by around 400 GeV. The low sensitivity at the low neutralino mass region is because its decay products in this region are very collimated and they do not pass the isolation requirements, resulting in a very low efficiency. The limits in Figure 7(f) are set for pair production of gluinos in the RPV model

	SRGGWZ-L	SRGGWZ-M	SRGGWZ-H	SRSSWZ-L	SRSSWZ-ML	SRSSWZ-MH	SRSSWZ-H
Observed	5	2	2	4	7	6	7
Total background	3.0 ± 0.7	3.5 ± 1.1	3.3 ± 0.6	5.2 ± 1.1	3.8 ± 0.8	3.9 ± 0.6	4.2 ± 0.7
$ZZ, W^{\pm}W^{\pm}, VVV$	0.09 ± 0.05	0.37 ± 0.15	0.47 ± 0.18	0.14 ± 0.07	0.09 ± 0.05	0.11 ± 0.05	0.15 ± 0.07
WZ	1.7 ± 0.5	1.6 ± 0.9	1.3 ± 0.5	2.0 ± 0.7	3.1 ± 0.7	3.1 ± 0.5	3.2 ± 0.7
$t\bar{t}W$	0.15 ± 0.09	0.26 ± 0.12	0.22 ± 0.07	0.12 ± 0.07	< 0.05	< 0.05	0.14 ± 0.03
$t\bar{t}Z$	0.24 ± 0.08	0.38 ± 0.22	0.15 ± 0.10	0.18 ± 0.10	0.38 ± 0.12	0.38 ± 0.11	0.31 ± 0.10
$t\bar{t}t\bar{t}$	0.02 ± 0.01	0.04 ± 0.02	< 0.02	< 0.02	< 0.02	< 0.02	< 0.02
Other SM processes	0.26 ± 0.17	0.53 ± 0.27	0.28 ± 0.15	0.36 ± 0.20	0.28 ± 0.15	0.25 ± 0.13	0.12 ± 0.07
Fake/non-prompt	0.56 ± 0.29	0.34 ± 0.24	0.85 ± 0.29	2.4 ± 0.8	< 0.3	< 0.3	0.24 ± 0.16
Charge-flip	< 0.02	0.03 ± 0.01	< 0.02	–	–	–	–

	SRGGSlep-L	SRGGSlep-M	SRGGSlep-H	SRSSSlep-L	SRSSSlep-ML	SRSSSlep-MH	SRSSSlep-H	SRSSSlep-H (loose)
Observed	2	5	0	9	3	6	0	10
Total background	2.9 ± 0.5	4.4 ± 0.8	3.0 ± 0.6	3.9 ± 0.8	3.6 ± 0.7	4.0 ± 0.6	0.99 ± 0.26	9.3 ± 1.9
WZ	1.39 ± 0.32	1.7 ± 0.4	1.6 ± 0.5	1.7 ± 0.5	1.6 ± 0.5	2.6 ± 0.5	0.71 ± 0.20	5.5 ± 1.3
$ZZ, W^{\pm}W^{\pm}, VVV$	0.14 ± 0.08	0.21 ± 0.11	0.18 ± 0.09	0.13 ± 0.07	0.23 ± 0.12	0.34 ± 0.17	0.04 ± 0.02	0.7 ± 0.4
$t\bar{t}W$	0.15 ± 0.08	0.31 ± 0.09	0.11 ± 0.05	0.14 ± 0.08	0.35 ± 0.07	0.30 ± 0.07	< 0.05	0.55 ± 0.29
$t\bar{t}Z$	0.15 ± 0.08	0.53 ± 0.18	0.15 ± 0.09	0.23 ± 0.14	0.19 ± 0.08	0.16 ± 0.09	0.05 ± 0.03	0.36 ± 0.22
$t\bar{t}t\bar{t}$	< 0.02	0.02 ± 0.01	0.02 ± 0.01	< 0.02	< 0.02	< 0.02	< 0.02	0.02 ± 0.01
Other SM processes	0.39 ± 0.23	0.8 ± 0.4	0.29 ± 0.18	0.7 ± 0.4	0.44 ± 0.25	0.17 ± 0.09	0.02 ± 0.03	0.34 ± 0.18
Fake/non-prompt	0.68 ± 0.32	0.8 ± 0.4	0.61 ± 0.19	0.96 ± 0.30	0.7 ± 0.4	0.46 ± 0.33	0.14 ± 0.14	1.9 ± 1.3
Charge-flip	–	–	–	–	–	–	–	–

	SRLQD	SRUDD-1b	SRUDD-2b	SRUDD-ge2b	SRUDD-ge3b
Observed	6	4	4	4	5
Total background	3.7 ± 0.9	2.9 ± 1.0	3.4 ± 0.9	4.8 ± 1.3	4.4 ± 1.4
WZ	0.38 ± 0.14	0.11 ± 0.06	0.09 ± 0.10	0.03 ± 0.02	< 0.02
$ZZ, W^{\pm}W^{\pm}, VVV$	0.62 ± 0.15	0.06 ± 0.03	0.08 ± 0.04	0.05 ± 0.02	< 0.02
$t\bar{t}W$	0.74 ± 0.24	0.75 ± 0.25	1.09 ± 0.28	1.21 ± 0.32	0.7 ± 0.4
$t\bar{t}Z$	0.20 ± 0.08	0.26 ± 0.11	0.25 ± 0.14	0.35 ± 0.20	0.24 ± 0.11
$t\bar{t}t\bar{t}$	0.13 ± 0.08	0.09 ± 0.06	0.17 ± 0.11	0.53 ± 0.31	1.4 ± 0.7
Other SM processes	0.52 ± 0.28	0.45 ± 0.25	0.62 ± 0.33	0.9 ± 0.5	0.7 ± 0.4
Fake/non-prompt	0.9 ± 0.7	1.1 ± 0.9	0.9 ± 0.7	1.4 ± 1.0	1.2 ± 0.9
Charge-flip	0.27 ± 0.14	0.11 ± 0.05	0.24 ± 0.10	0.24 ± 0.11	0.13 ± 0.06

Table 11: The number of observed data events and expected background contributions in all signal regions. Background categories shown as "–" denote that they cannot contribute to a given region. The displayed yields include all sources of statistical and systematic uncertainties. The individual uncertainties can be correlated or anticorrelated and therefore do not necessarily add up in quadrature.

where gluinos decay via top squarks into tbd final states when λ'' couplings are non-zero. The limits were obtained by using the statistical combination of the SRUDD-1b and SRUDD-ge2b, as it was found to provide the best expected sensitivity. Gluinos with masses up to 1.65 TeV are excluded for a top squark with masses below 1.45 TeV.

SR	σ_{vis}[fb]	S^{95}_{obs}	S^{95}_{exp}	CL_b	$p(s=0)$ (Z)
SRGGWZ-L	0.06	8.1	$5.2^{+2.2}_{-1.1}$	0.91	0.05 (1.64)
SRGGWZ-M	0.03	4.5	$5.2^{+2.1}_{-1.3}$	0.32	0.50 (0.00)
SRGGWZ-H	0.03	3.9	$5.0^{+2.0}_{-1.4}$	0.23	0.50 (0.00)
SRSSWZ-L	0.04	5.7	$6.1^{+2.3}_{-1.6}$	0.41	0.50 (0.00)
SRSSWZ-ML	0.07	10.4	$6.5^{+2.3}_{-1.5}$	0.94	0.02 (2.04)
SRSSWZ-MH	0.06	8.6	$5.3^{+2.0}_{-1.4}$	0.93	0.04 (1.74)
SRSSWZ-H	0.06	8.6	$5.4^{+2.5}_{-1.1}$	0.91	0.09 (1.32)
SRGGSlep-L	0.03	4.0	$4.7^{+2.0}_{-1.2}$	0.33	0.50 (0.00)
SRGGSlep-M	0.04	6.2	$5.8^{+2.2}_{-1.7}$	0.60	0.43 (0.17)
SRGGSlep-H	0.02	2.9	$4.7^{+2.0}_{-1.1}$	0.00	0.35 (0.39)
SRSSSlep-L	0.08	11.7	$5.6^{+2.4}_{-1.3}$	0.99	0.01 (2.33)
SRSSSlep-ML	0.03	4.8	$5.1^{+2.2}_{-1.3}$	0.43	0.50 (0.00)
SRSSSlep-MH	0.06	7.9	$5.4^{+2.3}_{-1.4}$	0.85	0.15 (1.06)
SRSSSlep-H	0.02	2.9	$3.5^{+1.3}_{-0.5}$	0.04	0.36 (0.35)
SRSSSlep-H (loose)	0.07	9.9	$8.1^{+3.3}_{-2.0}$	0.70	0.32 (0.46)
SRLQD	0.05	7.3	$5.3^{+2.3}_{-1.2}$	0.82	0.21 (0.81)
SRUDD-1b	0.05	6.6	$5.1^{+2.3}_{-1.1}$	0.77	0.21 (0.80)
SRUDD-2b	0.05	6.4	$5.2^{+2.4}_{-1.1}$	0.69	0.26 (0.66)
SRUDD-ge2b	0.04	5.8	$6.1^{+2.4}_{-1.4}$	0.44	0.50 (0.00)
SRUDD-ge3b	0.05	6.8	$6.1^{+2.4}_{-1.7}$	0.62	0.40 (0.24)

Table 12: Upper limits at 95% CL on the visible cross section (σ_{vis}), on the number of signal events (S^{95}_{obs}), and on the number of signal events given the expected number (and $\pm 1\sigma$ variations of the expectation) of background events. (S^{95}_{exp}). The last two columns indicate the CL_b value, i.e. the confidence level observed for the background-only hypothesis, the discovery p-value ($p(s=0)$) and its associated significance Z.

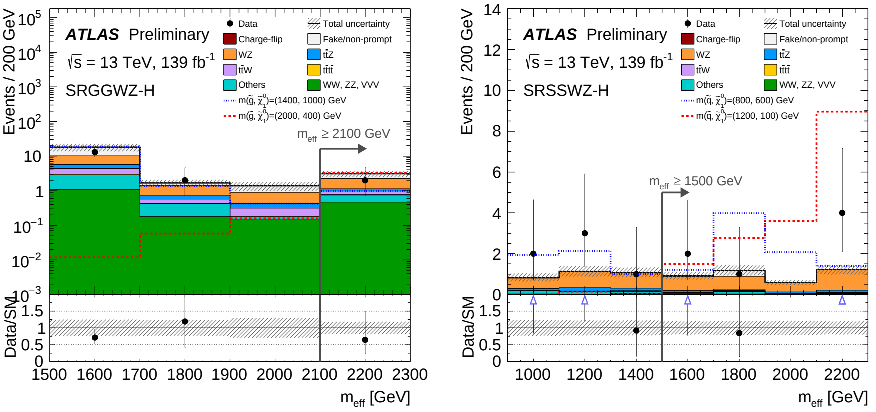

(a) SRGGWZ-H

(b) SRSSWZ-H

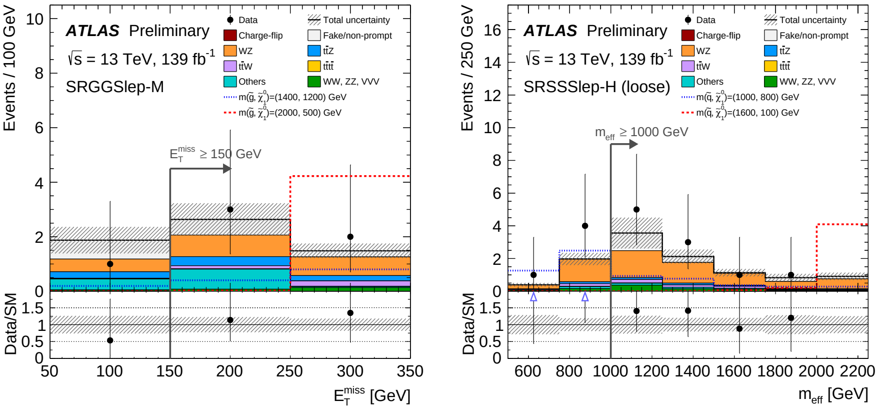

(c) SRGGSlep-M

(d) SRSSSlep-H (loose)

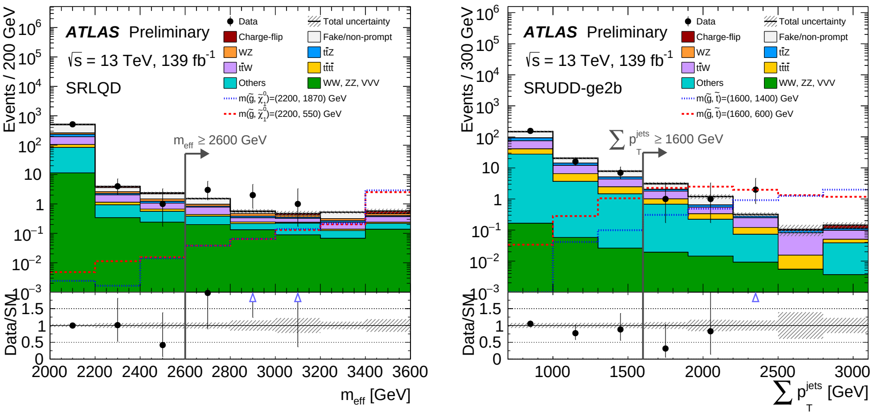

(e) SRLQD

(f) SRUDD-ge2b

Figure 6: Distributions of the data and estimated background after the background-only fit for the signal regions a) SRGGWZ-H, b) SRSSWZ-H, c) SRGGSlep-M, d) SRSSSlep-H (loose), e) SRLQD, and f) SRUDD-ge2b. All SRs selections but the one on the quantity shown are applied. The line with an arrow indicates the requirement used in the respective signal region. Distributions of two signal hypothesis for the concerned model are also shown. The bins displayed above the signal region requirement correspond to the binning used in the exclusion fit. All uncertainties are included in the uncertainty band. Overflow (underflow) events, where present, are included in the last (first) bin.

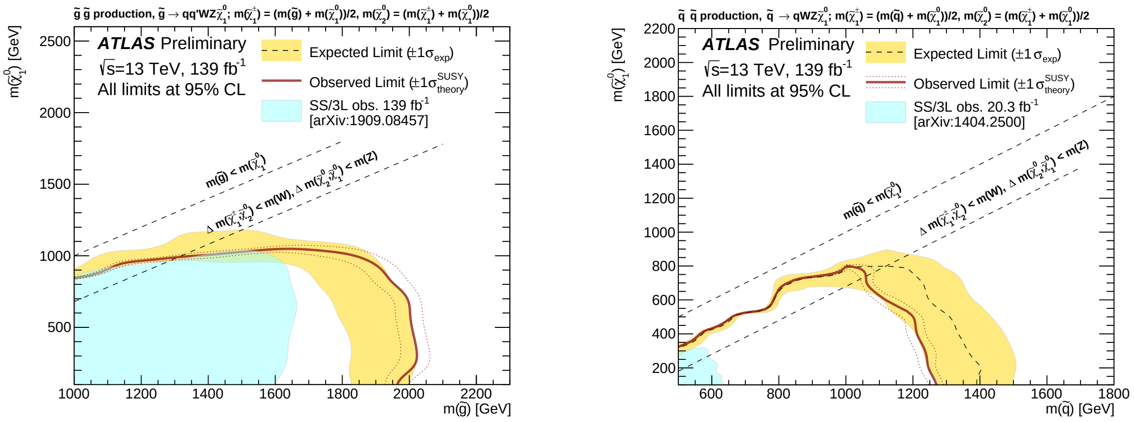

(a) $\tilde{g} \to qq'WZ\tilde{\chi}_1^0$

(b) $\tilde{q} \to q'WZ\tilde{\chi}_1^0$

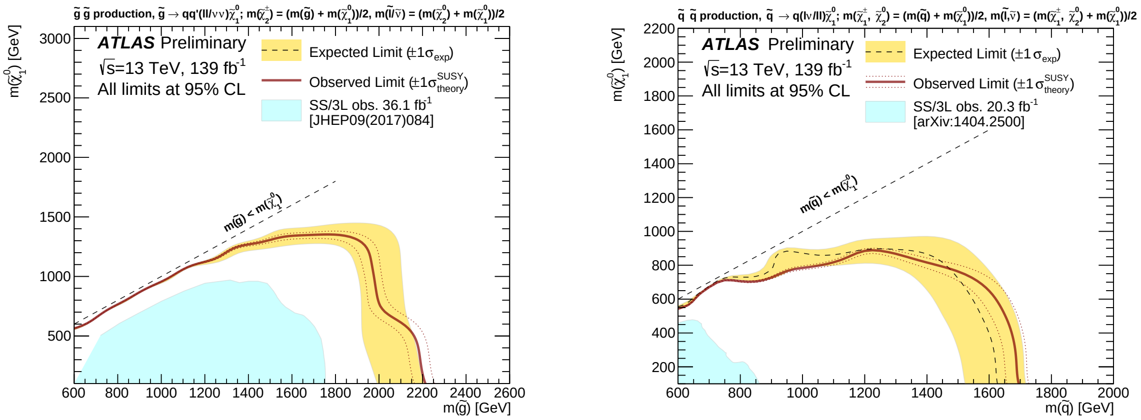

(c) $\tilde{g} \to q\bar{q}(\ell\ell/\nu\nu)\tilde{\chi}_1^0$

(d) $\tilde{q} \to q(\ell\nu/\ell\ell/\nu\nu)\tilde{\chi}_1^0$

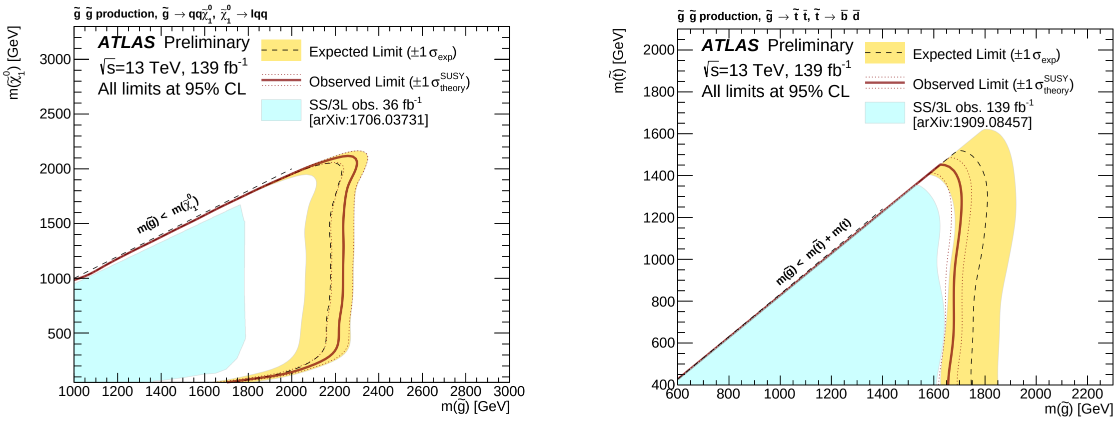

(e) $\tilde{g} \to q\bar{q}\tilde{\chi}_1^0, \tilde{\chi}_1^0 \to \ell qq$

(f) $\tilde{g} \to \bar{t}t, \tilde{t} \to \bar{b}\bar{d}$

Figure 7: Observed (red line) and expected (black dashed line) exclusion regions at 95% CL on the $\tilde{g}$, $\tilde{q}$, $\tilde{\chi}_1^0$ and $\tilde{t}$ masses obtained for the models shown in Figure 1. The yellow band shows the $\pm 1\sigma$ variation on the expected limits. The red dotted lines around the observed limit illustrate the change in the observed limit as the nominal signal cross-section is scaled up and down by the theoretical uncertainty. The light blue shaded area indicates the observed limits obtained by previous ATLAS searches.

11 Conclusion

A search for pair production of squarks or gluinos decaying via sleptons or weak bosons in final states with two same-sign or at least three leptons is presented. The search makes use of 139 fb^{-1} of proton–proton collision data collected by the ATLAS detector at the LHC at a centre-of-mass energy of 13 TeV.

No significant excess of events over the Standard Model expectation is observed. The results are interpreted in the context of several supersymmetric simplified models featuring gluino and squark production in R-parity-conserving and R-parity-violating scenarios. Lower limits on particle masses are derived at 95% confidence level for these models, reaching up to 2.2 TeV for gluinos and 1.7 TeV for squarks, raising the exclusion limits beyond those from previous similar searches made by ATLAS. Improved analysis techniques, the inclusion of a control region for the WZ+jets background, and a significantly larger dataset (when applicable) contributed to this improvement. Model-independent limits on the cross-section of a possible signal contribution to the signal regions defined in this search are also set.

References

[1] ATLAS Collaboration, *The ATLAS Experiment at the CERN Large Hadron Collider*, JINST **3** (2008) S08003 (cit. on pp. 2, 3).

[2] L. Evans and P. Bryant, *LHC Machine*, JINST **3** (2008) S08001 (cit. on p. 2).

[3] J. Alwall et al., *The automated computation of tree-level and next-to-leading order differential cross sections, and their matching to parton shower simulations*, JHEP **07** (2014) 079, arXiv: `1405.0301 [hep-ph]` (cit. on pp. 2, 7).

[4] A. De Simone, O. Matsedonskyi, R. Rattazzi and A. Wulzer, *A First Top Partner Hunter's Guide*, JHEP **04** (2013) 004, arXiv: `1211.5663 [hep-ph]` (cit. on p. 2).

[5] B. Fuks, M. Nemevšek and R. Ruiz, *Doubly Charged Higgs Boson Production at Hadron Colliders*, Phys. Rev. D **101** (2020) 075022, arXiv: `1912.08975 [hep-ph]` (cit. on p. 2).

[6] R. M. Barnett, J. F. Gunion and H. E. Haber, *Discovering supersymmetry with like sign dileptons*, Phys. Lett. B **315** (1993) 349, arXiv: `hep-ph/9306204` (cit. on p. 2).

[7] ATLAS Collaboration, *Search for anomalous production of prompt like-sign lepton pairs at $\sqrt{s} = 7$ TeV with the ATLAS detector*, JHEP **12** (2012) 007, arXiv: `1210.4538 [hep-ex]` (cit. on p. 2).

[8] CMS Collaboration, *Search for new physics in events with same-sign dileptons and b-tagged jets in pp collisions at $\sqrt{s} = 7$ TeV*, JHEP **08** (2012) 110, arXiv: `1205.3933 [hep-ex]` (cit. on p. 2).

[9] CDF Collaboration, *Inclusive Search for Anomalous Production of High-p_T Like-Sign Lepton Pairs in $p\overline{p}$ Collisions at $\sqrt{s} = 1.8$ TeV*, Phys. Rev. Lett. **93** (6 2004) 061802, URL: `https://link.aps.org/doi/10.1103/PhysRevLett.93.061802` (cit. on p. 2).

[10] Y. Golfand and E. Likhtman, *Extension of the Algebra of Poincare Group Generators and Violation of P Invariance*, JETP Lett. **13** (1971) 323, [Pisma Zh. Eksp. Teor. Fiz. **13** (1971) 452] (cit. on p. 2).

[11] D. Volkov and V. Akulov, *Is the neutrino a goldstone particle?*, Phys. Lett. B **46** (1973) 109 (cit. on p. 2).

[12] J. Wess and B. Zumino, *Supergauge transformations in four dimensions*, Nucl. Phys. B **70** (1974) 39 (cit. on p. 2).

[13] J. Wess and B. Zumino, *Supergauge invariant extension of quantum electrodynamics*, Nucl. Phys. B **78** (1974) 1 (cit. on p. 2).

[14] S. Ferrara and B. Zumino, *Supergauge invariant Yang-Mills theories*, Nucl. Phys. B **79** (1974) 413 (cit. on p. 2).

[15] A. Salam and J. Strathdee, *Super-symmetry and non-Abelian gauges*, Phys. Lett. B **51** (1974) 353 (cit. on p. 2).

[16] P. Fayet, *Supersymmetry and weak, electromagnetic and strong interactions*, Phys. Lett. B **64** (1976) 159 (cit. on p. 2).

[17] P. Fayet, *Spontaneously broken supersymmetric theories of weak, electromagnetic and strong interactions*, Phys. Lett. B **69** (1977) 489 (cit. on p. 2).

[18] P. Fayet, *Supergauge Invariant Extension of the Higgs Mechanism and a Model for the Electron and Its Neutrino*, Nucl. Phys. B **90** (1975) 104 (cit. on p. 2).

[19] A. Canepa, T. Han and X. Wang, *The Search for Electroweakinos*, Ann. Rev. Nucl. Part. Sci. **70** (2020) 425, arXiv: `2003.05450 [hep-ph]` (cit. on pp. 2, 5).

[20] G. R. Farrar and P. Fayet, *Phenomenology of the production, decay, and detection of new hadronic states associated with supersymmetry*, Phys. Lett. B **76** (1978) 575 (cit. on p. 2).

[21] H. Goldberg, *Constraint on the Photino Mass from Cosmology*, Phys. Rev. Lett. **50** (1983) 1419 (cit. on p. 2), Erratum: Phys. Rev. Lett. **103** (2009) 099905.

[22] J. Ellis, J. Hagelin, D. V. Nanopoulos, K. A. Olive and M. Srednicki, *Supersymmetric relics from the big bang*, Nucl. Phys. B **238** (1984) 453 (cit. on p. 2).

[23] L. Girardello and M. T. Grisaru, *Soft Breaking of Supersymmetry*, Nucl. Phys. B **194** (1982) 65 (cit. on p. 2).

[24] H. K. Dreiner, *An Introduction to explicit R-parity violation*, Adv. Ser. Direct. High Energy Phys. **21** (2010) 565, ed. by G. L. Kane, arXiv: `hep-ph/9707435` (cit. on p. 2).

[25] ATLAS Collaboration, *Search for squarks and gluinos in final states with same-sign leptons and jets using* $139\,fb^{-1}$ *of data collected with the ATLAS detector*, JHEP **06** (2020) 046, arXiv: `1909.08457 [hep-ex]` (cit. on pp. 2, 5, 6, 13, 14).

[26] CMS Collaboration, *Search for physics beyond the standard model in events with jets and two same-sign or at least three charged leptons in proton–proton collisions at* $\sqrt{s} = 13\,TeV$, Eur. Phys. J. C **80** (2020) 752, arXiv: `2001.10086 [hep-ex]` (cit. on pp. 2, 5).

[27] ATLAS Collaboration, *Summary of the searches for squarks and gluinos using* $\sqrt{s} = 8\,TeV\ pp$ *collisions with the ATLAS experiment at the LHC*, JHEP **10** (2015) 054, arXiv: `1507.05525 [hep-ex]` (cit. on pp. 2, 5).

[28] ATLAS Collaboration, *ATLAS Insertable B-Layer: Technical Design Report*, ATLAS-TDR-19; CERN-LHCC-2010-013, 2010, URL: `https://cds.cern.ch/record/1291633` (cit. on p. 3), Addendum: ATLAS-TDR-19-ADD-1; CERN-LHCC-2012-009, 2012, URL: `https://cds.cern.ch/record/1451888`.

[29] B. Abbott et al., *Production and integration of the ATLAS Insertable B-Layer*, JINST **13** (2018) T05008, arXiv: `1803.00844 [physics.ins-det]` (cit. on p. 3).

[30] ATLAS Collaboration, *Performance of the ATLAS trigger system in 2015*, Eur. Phys. J. C **77** (2017) 317, arXiv: `1611.09661 [hep-ex]` (cit. on p. 3).

[31] ATLAS Collaboration, *The ATLAS Collaboration Software and Firmware*, ATL-SOFT-PUB-2021-001, 2021, URL: `https://cds.cern.ch/record/2767187` (cit. on p. 4).

[32] ATLAS Collaboration, *Search for squarks and gluinos in final states with jets and missing transverse momentum using* $139\,fb^{-1}$ *of* $\sqrt{s} = 13\,TeV\ pp$ *collision data with the ATLAS detector*, JHEP **02** (2021) 143, arXiv: `2010.14293 [hep-ex]` (cit. on p. 4).

[33] ATLAS Collaboration, *Search for squarks and gluinos in final states with one isolated lepton, jets, and missing transverse momentum at* $\sqrt{s} = 13\,TeV$ *with the ATLAS detector*, Eur. Phys. J. C **81** (2021) 600, arXiv: `2101.01629 [hep-ex]` (cit. on p. 4), Erratum: Eur. Phys. J. C **81** (2021) 956.

[34] ATLAS Collaboration, *Searches for new phenomena in events with two leptons, jets, and missing transverse momentum in* 139 fb^{-1} *of* $\sqrt{s} = 13$ *TeV* pp *collisions with the ATLAS detector*, (2022), arXiv: 2204.13072 [hep-ex] (cit. on p. 4).

[35] J. Alwall, M.-P. Le, M. Lisanti and J. G. Wacker, *Searching for directly decaying gluinos at the Tevatron*, Phys. Lett. B **666** (2008) 34, arXiv: 0803.0019 [hep-ph] (cit. on p. 5).

[36] J. Alwall, P. Schuster and N. Toro, *Simplified models for a first characterization of new physics at the LHC*, Phys. Rev. D **79** (2009) 075020, arXiv: 0810.3921 [hep-ph] (cit. on p. 5).

[37] D. Alves et al., *Simplified models for LHC new physics searches*, J. Phys. G **39** (2012) 105005, arXiv: 1105.2838 [hep-ph] (cit. on p. 5).

[38] S. P. Martin, *A Supersymmetry Primer*, Adv. Ser. Direct. High Energy Phys. **18** (1998) 1, arXiv: hep-ph/9709356 (cit. on p. 5).

[39] M. Dine and W. Fischler, *A phenomenological model of particle physics based on supersymmetry*, Phys. Lett. B **110** (1982) 227 (cit. on p. 5).

[40] L. Alvarez-Gaumé, M. Claudson and M. B. Wise, *Low-energy supersymmetry*, Nucl. Phys. B **207** (1982) 96 (cit. on p. 5).

[41] C. R. Nappi and B. A. Ovrut, *Supersymmetric extension of the SU(3) x SU(2) x U(1) model*, Phys. Lett. B **113** (1982) 175 (cit. on p. 5).

[42] ATLAS Collaboration, *Search for squarks and gluinos in events with an isolated lepton, jets, and missing transverse momentum at* $\sqrt{s} = 13$ *TeV with the ATLAS detector*, Phys. Rev. D **96** (2017) 112010, arXiv: 1708.08232 [hep-ex] (cit. on p. 5).

[43] ATLAS Collaboration, *Search for new phenomena in final states with large jet multiplicities and missing transverse momentum using* $\sqrt{s} = 13$ *TeV proton–proton collisions recorded by ATLAS in Run 2 of the LHC*, JHEP **10** (2020) 062, arXiv: 2008.06032 [hep-ex] (cit. on p. 5).

[44] ATLAS Collaboration, *Further search for supersymmetry at* $\sqrt{s} = 7$ *TeV in final states with jets, missing transverse momentum and isolated leptons with the ATLAS detector*, Phys. Rev. D **86** (2012) 092002, arXiv: 1208.4688 [hep-ex] (cit. on p. 5).

[45] ATLAS Collaboration, *Search for supersymmetry with jets, missing transverse momentum and at least one hadronically decaying* τ *lepton in proton–proton collisions at* $\sqrt{s} = 7$ *TeV with the ATLAS detector*, Phys. Lett. B **714** (2012) 197, arXiv: 1204.3852 [hep-ex] (cit. on p. 5).

[46] ATLAS Collaboration, *Search for events with large missing transverse momentum, jets, and at least two tau leptons in* 7 *TeV proton–proton collision data with the ATLAS detector*, Phys. Lett. B **714** (2012) 180, arXiv: 1203.6580 [hep-ex] (cit. on p. 5).

[47] ATLAS Collaboration, *Search for electroweak production of charginos and sleptons decaying into final states with two leptons and missing transverse momentum in* $\sqrt{s} = 13$ *TeV* pp *collisions using the ATLAS detector*, Eur. Phys. J. C **80** (2020) 123, arXiv: 1908.08215 [hep-ex] (cit. on p. 5).

[48] ATLAS Collaboration, *Search for direct stau production in events with two hadronic* τ*-leptons in* $\sqrt{s} = 13$ *TeV* pp *collisions with the ATLAS detector*, Phys. Rev. D **101** (2020) 032009, arXiv: 1911.06660 [hep-ex] (cit. on p. 5).

[49] CMS Collaboration, *Search for supersymmetric partners of electrons and muons in proton–proton collisions at $\sqrt{s} = 13$ TeV*, Phys. Lett. B **790** (2019) 140, arXiv: `1806.05264 [hep-ex]` (cit. on p. 5).

[50] CMS Collaboration, *Search for direct pair production of supersymmetric partners of τ leptons in the final state with two hadronically decaying τ leptons and missing transverse momentum in proton–proton collisions at $\sqrt{s} = 13$ TeV*, (2022), arXiv: `2207.02254 [hep-ex]` (cit. on p. 5).

[51] R. Barbier et al., *R-parity violating supersymmetry*, Phys. Rept. **420** (2005) 1, arXiv: `hep-ph/0406039` (cit. on p. 5).

[52] ATLAS Collaboration, *Search for R-parity-violating supersymmetry in a final state containing leptons and many jets with the ATLAS experiment using $\sqrt{s} = 13$ TeV proton–proton collision data*, Eur. Phys. J. C **81** (2021) 1023, arXiv: `2106.09609 [hep-ex]` (cit. on p. 5).

[53] B. C. Allanach and B. Gripaios, *Hide and Seek With Natural Supersymmetry at the LHC*, JHEP **05** (2012) 062, arXiv: `1202.6616 [hep-ph]` (cit. on p. 5).

[54] ATLAS Collaboration, *Search for supersymmetry in final states with two same-sign or three leptons and jets using 36 fb^{-1} of $\sqrt{s} = 13$ TeV pp collision data with the ATLAS detector*, JHEP **09** (2017) 084, arXiv: `1706.03731 [hep-ex]` (cit. on pp. 5, 13), Erratum: JHEP **08** (2019) 121.

[55] ATLAS Collaboration, *A search for pair-produced resonances in four-jet final states at $\sqrt{s} = 13$ TeV with the ATLAS detector*, Eur. Phys. J. C **78** (2018) 250, arXiv: `1710.07171 [hep-ex]` (cit. on p. 6).

[56] ATLAS Collaboration, *ATLAS data quality operations and performance for 2015–2018 data-taking*, JINST **15** (2020) P04003, arXiv: `1911.04632 [physics.ins-det]` (cit. on p. 6).

[57] ATLAS Collaboration, *Luminosity determination in pp collisions at $\sqrt{s} = 13$ TeV using the ATLAS detector at the LHC*, ATLAS-CONF-2019-021, 2019, URL: `https://cds.cern.ch/record/2677054` (cit. on p. 6).

[58] G. Avoni et al., *The new LUCID-2 detector for luminosity measurement and monitoring in ATLAS*, JINST **13** (2018) P07017 (cit. on pp. 6, 16).

[59] ATLAS Collaboration, *The ATLAS Simulation Infrastructure*, Eur. Phys. J. C **70** (2010) 823, arXiv: `1005.4568 [physics.ins-det]` (cit. on p. 6).

[60] GEANT4 Collaboration, S. Agostinelli et al., *Geant4 – a simulation toolkit*, Nucl. Instrum. Meth. A **506** (2003) 250 (cit. on p. 6).

[61] ATLAS Collaboration, *The simulation principle and performance of the ATLAS fast calorimeter simulation FastCaloSim*, ATL-PHYS-PUB-2010-013, 2010, URL: `https://cds.cern.ch/record/1300517` (cit. on p. 6).

[62] ATLAS Collaboration, *Modelling of rare top quark processes at $\sqrt{s} = 13$ TeV in ATLAS*, ATL-PHYS-PUB-2020-024, 2020, URL: `https://cds.cern.ch/record/2730584` (cit. on p. 7).

[63] E. Bothmann et al., *Event generation with Sherpa 2.2*, SciPost Phys. **7** (2019) 034, arXiv: `1905.09127 [hep-ph]` (cit. on p. 7).

[64] S. Schumann and F. Krauss,
A parton shower algorithm based on Catani–Seymour dipole factorisation, JHEP **03** (2008) 038,
arXiv: `0709.1027 [hep-ph]` (cit. on p. 7).

[65] R. D. Ball et al., *Parton distributions for the LHC run II*, JHEP **04** (2015) 040,
arXiv: `1410.8849 [hep-ph]` (cit. on p. 7).

[66] F. Buccioni et al., *OpenLoops 2*, Eur. Phys. J. C **79** (2019) 866, arXiv: `1907.13071 [hep-ph]`
(cit. on p. 7).

[67] F. Cascioli, P. Maierhöfer and S. Pozzorini, *Scattering Amplitudes with Open Loops*,
Phys. Rev. Lett. **108** (2012) 111601, arXiv: `1111.5206 [hep-ph]` (cit. on p. 7).

[68] A. Denner, S. Dittmaier and L. Hofer,
Collier: A fortran-based complex one-loop library in extended regularizations,
Comput. Phys. Commun. **212** (2017) 220, arXiv: `1604.06792 [hep-ph]` (cit. on p. 7).

[69] T. Gleisberg and S. Höche, *Comix, a new matrix element generator*, JHEP **12** (2008) 039,
arXiv: `0808.3674 [hep-ph]` (cit. on p. 7).

[70] T. Sjöstrand, S. Mrenna and P. Skands, *A brief introduction to PYTHIA 8.1*,
Comput. Phys. Commun. **178** (2008) 852, arXiv: `0710.3820 [hep-ph]` (cit. on p. 7).

[71] ATLAS Collaboration, *ATLAS Pythia 8 tunes to* 7 *TeV data*, ATL-PHYS-PUB-2014-021, 2014,
URL: `https://cds.cern.ch/record/1966419` (cit. on p. 7).

[72] ATLAS Collaboration,
Modelling of the $t\bar{t}H$ and $t\bar{t}V$ $(V = W, Z)$ processes for $\sqrt{s}$ = 13 *TeV ATLAS analyses*,
ATL-PHYS-PUB-2016-005, 2016, URL: `https://cds.cern.ch/record/2120826`
(cit. on p. 7).

[73] D. de Florian et al.,
Handbook of LHC Higgs Cross Sections: 4. Deciphering the Nature of the Higgs Sector, (2016),
arXiv: `1610.07922 [hep-ph]` (cit. on p. 7).

[74] S. Frixione, E. Laenen, P. Motylinski and B. R. Webber, *Angular correlations of lepton pairs from vector boson and top quark decays in Monte Carlo simulations*, JHEP **04** (2007) 081,
arXiv: `hep-ph/0702198` (cit. on p. 7).

[75] P. Artoisenet, R. Frederix, O. Mattelaer and R. Rietkerk,
Automatic spin-entangled decays of heavy resonances in Monte Carlo simulations,
JHEP **03** (2013) 015, arXiv: `1212.3460 [hep-ph]` (cit. on p. 7).

[76] ATLAS Collaboration, *Multi-Boson Simulation for* 13 *TeV ATLAS Analyses*,
ATL-PHYS-PUB-2017-005, 2017, URL: `https://cds.cern.ch/record/2261933`
(cit. on pp. 6, 7).

[77] ATLAS Collaboration, *Studies on top-quark Monte Carlo modelling for Top2016*,
ATL-PHYS-PUB-2016-020, 2016, URL: `https://cds.cern.ch/record/2216168`
(cit. on p. 7).

[78] S. Frixione, G. Ridolfi and P. Nason,
A positive-weight next-to-leading-order Monte Carlo for heavy flavour hadroproduction,
JHEP **09** (2007) 126, arXiv: `0707.3088 [hep-ph]` (cit. on p. 7).

[79] P. Nason, *A new method for combining NLO QCD with shower Monte Carlo algorithms*,
JHEP **11** (2004) 040, arXiv: `hep-ph/0409146` (cit. on p. 7).

[80] S. Frixione, P. Nason and C. Oleari,
Matching NLO QCD computations with parton shower simulations: the POWHEG method,
JHEP **11** (2007) 070, arXiv: `0709.2092 [hep-ph]` (cit. on p. 7).

[81] S. Alioli, P. Nason, C. Oleari and E. Re, *A general framework for implementing NLO calculations in shower Monte Carlo programs: the POWHEG BOX*, JHEP **06** (2010) 043,
arXiv: `1002.2581 [hep-ph]` (cit. on p. 7).

[82] T. Sjöstrand et al., *An introduction to PYTHIA 8.2*, Comput. Phys. Commun. **191** (2015) 159,
arXiv: `1410.3012 [hep-ph]` (cit. on p. 7).

[83] E. Re,
Single-top Wt-channel production matched with parton showers using the POWHEG method,
Eur. Phys. J. C **71** (2011) 1547, arXiv: `1009.2450 [hep-ph]` (cit. on p. 7).

[84] J. Campbell, T. Neumann and Z. Sullivan, *Single-top-quark production in the t-channel at NNLO*,
JHEP **02** (2021) 040, arXiv: `2012.01574 [hep-ph]` (cit. on p. 7).

[85] R. D. Ball et al., *The PDF4LHC21 combination of global PDF fits for the LHC Run III*,
J. Phys. G **49** (2022) 080501, arXiv: `2203.05506 [hep-ph]` (cit. on p. 7).

[86] N. Kidonakis and N. Yamanaka,
Higher-order corrections for tW production at high-energy hadron colliders, JHEP **05** (2021) 278,
arXiv: `2102.11300 [hep-ph]` (cit. on p. 7).

[87] ATLAS Collaboration, *ATLAS simulation of boson plus jets processes in Run 2*,
ATL-PHYS-PUB-2017-006, 2017, URL: `https://cds.cern.ch/record/2261937`
(cit. on p. 7).

[88] C. Anastasiou, L. Dixon, K. Melnikov and F. Petriello, *High-precision QCD at hadron colliders: Electroweak gauge boson rapidity distributions at next-to-next-to leading order*,
Phys. Rev. D **69** (2004) 094008, arXiv: `hep-ph/0312266` (cit. on p. 7).

[89] D. J. Lange, *The EvtGen particle decay simulation package*,
Nucl. Instrum. Meth. A **462** (2001) 152 (cit. on p. 6).

[90] L. Lönnblad and S. Prestel, *Matching tree-level matrix elements with interleaved showers*,
JHEP **03** (2012) 019, arXiv: `1109.4829 [hep-ph]` (cit. on p. 7).

[91] W. Beenakker, C. Borschensky, M. Krämer, A. Kulesza and E. Laenen,
NNLL-fast: predictions for coloured supersymmetric particle production at the LHC with threshold and Coulomb resummation, JHEP **12** (2016) 133, arXiv: `1607.07741 [hep-ph]` (cit. on p. 7).

[92] W. Beenakker et al., *NNLL resummation for squark and gluino production at the LHC*,
JHEP **12** (2014) 023, arXiv: `1404.3134 [hep-ph]` (cit. on p. 7).

[93] W. Beenakker et al.,
Towards NNLL resummation: hard matching coefficients for squark and gluino hadroproduction,
JHEP **10** (2013) 120, arXiv: `1304.6354 [hep-ph]` (cit. on p. 7).

[94] W. Beenakker et al., *NNLL resummation for squark-antisquark pair production at the LHC*,
JHEP **01** (2012) 076, arXiv: `1110.2446 [hep-ph]` (cit. on p. 7).

[95] W. Beenakker et al., *Soft-gluon resummation for squark and gluino hadroproduction*,
JHEP **12** (2009) 041, arXiv: `0909.4418 [hep-ph]` (cit. on p. 7).

[96] A. Kulesza and L. Motyka, *Soft gluon resummation for the production of gluino-gluino and squark-antisquark pairs at the LHC*, Phys. Rev. D **80** (2009) 095004, arXiv: `0905.4749 [hep-ph]` (cit. on p. 7).

[97] A. Kulesza and L. Motyka, *Threshold Resummation for Squark-Antisquark and Gluino-Pair Production at the LHC*, Phys. Rev. Lett. **102** (2009) 111802, arXiv: `0807.2405 [hep-ph]` (cit. on p. 7).

[98] W. Beenakker, R. Höpker, M. Spira and P. Zerwas, *Squark and gluino production at hadron colliders*, Nucl. Phys. B **492** (1997) 51, arXiv: `hep-ph/9610490` (cit. on p. 7).

[99] J. Butterworth et al., *PDF4LHC recommendations for LHC Run II*, J. Phys. G **43** (2016) 023001, arXiv: `1510.03865 [hep-ph]` (cit. on p. 7).

[100] T. Cornelissen et al., *The new ATLAS track reconstruction (NEWT)*, Journal of Physics: Conference Series **119** (2008) 032014 (cit. on p. 7).

[101] ATLAS Collaboration, *Performance of the ATLAS Inner Detector Track and Vertex Reconstruction in High Pile-Up LHC Environment*, ATLAS-CONF-2012-042, 2012, URL: `https://cds.cern.ch/record/1435196` (cit. on p. 7).

[102] A. Salzburger, *Optimisation of the ATLAS Track Reconstruction Software for Run-2*, J. Phys. Conf. Ser. **664** (2015) 072042, URL: `https://cds.cern.ch/record/2018442` (cit. on p. 7).

[103] ATLAS Collaboration, *Reconstruction of primary vertices at the ATLAS experiment in Run 1 proton–proton collisions at the LHC*, Eur. Phys. J. C **77** (2017) 332, arXiv: `1611.10235 [hep-ex]` (cit. on p. 7).

[104] ATLAS Collaboration, *Vertex Reconstruction Performance of the ATLAS Detector at* $\sqrt{s} = 13$ *TeV*, ATL-PHYS-PUB-2015-026, 2015, URL: `https://cds.cern.ch/record/2037717` (cit. on p. 7).

[105] ATLAS Collaboration, *Development of ATLAS Primary Vertex Reconstruction for LHC Run 3*, ATL-PHYS-PUB-2019-015, 2019, URL: `https://cds.cern.ch/record/2670380` (cit. on p. 7).

[106] ATLAS Collaboration, *Alignment of the ATLAS Inner Detector in Run-2*, Eur. Phys. J. C **80** (2020) 1194, arXiv: `2007.07624 [hep-ex]` (cit. on p. 7).

[107] M. Cacciari, G. P. Salam and G. Soyez, *FastJet user manual*, Eur. Phys. J. C **72** (2012) 1896, arXiv: `1111.6097 [hep-ph]` (cit. on p. 8).

[108] M. Cacciari, G. P. Salam and G. Soyez, *The anti-*k_t *jet clustering algorithm*, JHEP **04** (2008) 063, arXiv: `0802.1189 [hep-ph]` (cit. on p. 8).

[109] ATLAS Collaboration, *Jet energy scale and resolution measured in proton–proton collisions at* $\sqrt{s} = 13$ *TeV with the ATLAS detector*, Eur. Phys. J. C **81** (2020) 689, arXiv: `2007.02645 [hep-ex]` (cit. on pp. 8, 16).

[110] ATLAS Collaboration, *Jet reconstruction and performance using particle flow with the ATLAS Detector*, Eur. Phys. J. C **77** (2017) 466, arXiv: `1703.10485 [hep-ex]` (cit. on p. 8).

[111] ATLAS Collaboration, *Topological cell clustering in the ATLAS calorimeters and its performance in LHC Run 1*, Eur. Phys. J. C **77** (2017) 490, arXiv: `1603.02934 [hep-ex]` (cit. on p. 8).

[112] ATLAS Collaboration, *Performance of pile-up mitigation techniques for jets in pp collisions at $\sqrt{s} = 8$ TeV using the ATLAS detector*, Eur. Phys. J. C **76** (2016) 581, arXiv: `1510.03823 [hep-ex]` (cit. on p. 8).

[113] ATLAS Collaboration, *Selection of jets produced in 13 TeV proton–proton collisions with the ATLAS detector*, ATLAS-CONF-2015-029, 2015, URL: `https://cds.cern.ch/record/2037702` (cit. on p. 8).

[114] ATLAS Collaboration, *ATLAS flavour-tagging algorithms for the LHC Run 2 pp collision dataset*, (2022), arXiv: `2211.16345 [physics.data-an]` (cit. on p. 8).

[115] ATLAS Collaboration, *Muon reconstruction and identification efficiency in ATLAS using the full Run 2 pp collision data set at $\sqrt{s} = 13$ TeV*, Eur. Phys. J. C **81** (2021) 578, arXiv: `2012.00578 [hep-ex]` (cit. on pp. 8, 16).

[116] ATLAS Collaboration, *Studies of the muon momentum calibration and performance of the ATLAS detector with pp collisions at $\sqrt{s}$=13 TeV*, (2022), arXiv: `2212.07338 [hep-ex]` (cit. on pp. 8, 16).

[117] ATLAS Collaboration, *Electron and photon performance measurements with the ATLAS detector using the 2015–2017 LHC proton–proton collision data*, JINST **14** (2019) P12006, arXiv: `1908.00005 [hep-ex]` (cit. on pp. 8, 9, 13, 16).

[118] ATLAS Collaboration, *Electron and photon energy calibration with the ATLAS detector using 2015–2016 LHC proton–proton collision data*, JINST **14** (2019) P03017, arXiv: `1812.03848 [hep-ex]` (cit. on p. 8).

[119] ATLAS Collaboration, *E_T^{miss} performance in the ATLAS detector using 2015–2016 LHC pp collisions*, ATLAS-CONF-2018-023, 2018, URL: `https://cds.cern.ch/record/2625233` (cit. on pp. 9, 16).

[120] ATLAS Collaboration, *Performance of electron and photon triggers in ATLAS during LHC Run 2*, Eur. Phys. J. C **80** (2020) 47, arXiv: `1909.00761 [hep-ex]` (cit. on pp. 9, 14, 16).

[121] ATLAS Collaboration, *Performance of the ATLAS muon triggers in Run 2*, JINST **15** (2020) P09015, arXiv: `2004.13447 [hep-ex]` (cit. on pp. 9, 16).

[122] ATLAS Collaboration, *Performance of the missing transverse momentum triggers for the ATLAS detector during Run-2 data taking*, JHEP **08** (2020) 080, arXiv: `2005.09554 [hep-ex]` (cit. on pp. 9, 16).

[123] ATLAS Collaboration, *Object-based missing transverse momentum significance in the ATLAS Detector*, ATLAS-CONF-2018-038, 2018, URL: `https://cds.cern.ch/record/2630948` (cit. on p. 10).

[124] ATLAS Collaboration, *Observation of electroweak $W^{\pm}Z$ boson pair production in association with two jets in pp collisions at $\sqrt{s} = 13$ TeV with the ATLAS detector*, Phys. Lett. B **793** (2019) 469, arXiv: `1812.09740 [hep-ex]` (cit. on p. 12).

[125] ATLAS Collaboration, *Measurement of $W^{\pm}Z$ production cross sections and gauge boson polarisation in pp collisions at $\sqrt{s} = 13$ TeV with the ATLAS detector*, Eur. Phys. J. C **79** (2019) 535, arXiv: `1902.05759 [hep-ex]` (cit. on p. 12).

[126] ATLAS Collaboration, *Observation of Higgs boson production in association with a top quark pair at the LHC with the ATLAS detector*, Phys. Lett. B **784** (2018) 173, arXiv: `1806.00425 [hep-ex]` (cit. on p. 13).

[127] ATLAS Collaboration, *Search for direct production of winos and higgsinos in events with two same-sign or three leptons in pp collision data at 13 TeV with the ATLAS detector*, ATLAS-CONF-2022-057, 2022, URL: `https://cds.cern.ch/record/2826603` (cit. on p. 13).

[128] D0 Collaboration, *Extraction of the width of the W boson from measurements of $\sigma(p\bar{p} \to W + X) \times B(W \to e\nu)$ and $\sigma(p\bar{p} \to Z + X) \times B(Z \to ee)$ and their ratio*, Phys. Rev. D **61** (2000) 072001, arXiv: `hep-ex/9906025` (cit. on p. 13).

[129] ATLAS Collaboration, *Tools for estimating fake/non-prompt lepton backgrounds with the ATLAS detector at the LHC*, (2022), arXiv: `2211.16178 [hep-ex]` (cit. on p. 14).

[130] ATLAS Collaboration, *Electron reconstruction and identification in the ATLAS experiment using the 2015 and 2016 LHC proton–proton collision data at $\sqrt{s} = 13$ TeV*, Eur. Phys. J. C **79** (2019) 639, arXiv: `1902.04655 [hep-ex]` (cit. on p. 16).

[131] ATLAS Collaboration, *Electron efficiency measurements with the ATLAS detector using the 2015 LHC proton–proton collision data*, ATLAS-CONF-2016-024, 2016, URL: `https://cds.cern.ch/record/2157687` (cit. on p. 16).

[132] ATLAS Collaboration, *Forward jet vertex tagging using the particle flow algorithm*, ATL-PHYS-PUB-2019-026, 2019, URL: `https://cds.cern.ch/record/2683100` (cit. on p. 16).

[133] ATLAS Collaboration, *Jet energy scale measurements and their systematic uncertainties in proton–proton collisions at $\sqrt{s} = 13$ TeV with the ATLAS detector*, Phys. Rev. D **96** (2017) 072002, arXiv: `1703.09665 [hep-ex]` (cit. on p. 16).

[134] ATLAS Collaboration, *ATLAS b-jet identification performance and efficiency measurement with $t\bar{t}$ events in pp collisions at $\sqrt{s} = 13$ TeV*, Eur. Phys. J. C **79** (2019) 970, arXiv: `1907.05120 [hep-ex]` (cit. on p. 16).

[135] ATLAS Collaboration, *Measurement of the c-jet mistagging efficiency in $t\bar{t}$ events using pp collision data at $\sqrt{s} = 13$ TeV collected with the ATLAS detector*, Eur. Phys. J. C **82** (2021) 95, arXiv: `2109.10627 [hep-ex]` (cit. on p. 16).

[136] ATLAS Collaboration, *Calibration of light-flavour b-jet mistagging rates using ATLAS proton–proton collision data at $\sqrt{s} = 13$ TeV*, ATLAS-CONF-2018-006, 2018, URL: `https://cds.cern.ch/record/2314418` (cit. on p. 16).

[137] L. A. Harland-Lang, A. D. Martin, P. Motylinski and R. S. Thorne, *Parton distributions in the LHC era: MMHT 2014 PDFs*, Eur. Phys. J. C **75** (2015) 204, arXiv: `1412.3989 [hep-ph]` (cit. on p. 16).

[138] S. Dulat et al., *New parton distribution functions from a global analysis of quantum chromodynamics*, Phys. Rev. D **93** (2016) 033006, arXiv: `1506.07443 [hep-ph]` (cit. on p. 16).

[139] R. D. Ball et al., *Parton distributions with LHC data*, Nucl. Phys. B **867** (2013) 244, arXiv: `1207.1303 [hep-ph]` (cit. on p. 16).

[140] M. Baak et al., *HistFitter software framework for statistical data analysis*, Eur. Phys. J. C **75** (2015) 153, arXiv: `1410.1280 [hep-ex]` (cit. on p. 17).

[141] T. Junk, *Confidence level computation for combining searches with small statistics*, Nucl. Instrum. Meth. A **434** (1999) 435, arXiv: `hep-ex/9902006` (cit. on p. 18).

[142] A. L. Read, *Presentation of search results: the CL_S technique*, J. Phys. G **28** (2002) 2693 (cit. on p. 18).

[143] G. Cowan, K. Cranmer, E. Gross and O. Vitells, *Asymptotic formulae for likelihood-based tests of new physics*, Eur. Phys. J. C **71** (2011) 1554, arXiv: `1007.1727 [physics.data-an]` (cit. on p. 19), Erratum: Eur. Phys. J. C **73** (2013) 2501.